New insights into combined surfzone and estuarine bathing hazards

Christopher Stokes[1], Timothy Poate[1], Gerd Masselink[1], Tim Scott[1], Steve Instance[2]

[1]School of Biological and Marine Sciences, University of Plymouth, PL4 8AA, England
[2] Royal National Lifeboat Institution, West Quay Road, Poole, Dorset, BH15 1HZ, England

Correspondence to: Christopher Stokes (christopher.stokes@plymouth.ac.uk)

Abstract. Rip currents are the single largest cause of beach safety incidents globally, but where an estuary mouth intersects a beach, additional flows are created that can exceed the speed of a typical rip current, significantly increasing the hazard level for bathers. However, there is a paucity of observations of surfzone currents at estuary mouth beaches, and our understanding and ability to predict how the bathing hazard varies under different wave and tide conditions is therefore limited. Using field observations and process-based XBeach modelling, we demonstrate how surfzone currents can be driven by combinations of estuary discharge and wave-driven rip currents under various combinations of wave and tide forcing. While previous studies have demonstrated the high hazard that rip currents pose, typically during lower stages of the tide, here we demonstrate that an estuary mouth beach can exhibit flows reaching 1.5 m/s – up to 50% stronger than typical rip current flows – with a high proportion (>60%) of simulated bathers exiting the surfzone during the upper half of the tidal cycle. The three-dimensional ebb shoal delta was found to strongly control surfzone currents by providing a conduit for estuary flows and acting as a nearshore bar system to generate wave-driven 'river channel rips'. Despite significant spatio-temporal variability in the position of the river channels on the beach face, it was found to be possible to hindcast the timing and severity of past bathing incidents from model simulations, providing a means to forewarn bathers of hazardous flows.

Introduction

Estuary mouth beaches are energetic environments where dynamic exchanges between marine and estuarine processes take place, resulting in complex hydrodynamics and a high degree of morphologic variability (Barnard and Warrick, 2010). For the present study we define them as wave-dominated beaches which feature an estuary that exits across the beach face, and distinguish them from *estuarine beaches*, which sit within enclosed estuary environments and where only fetch-limited, locally-generated waves are important (Nordstrom, 1992). Estuary mouth beaches are ubiquitous across the globe (Figure 1), with examples in meso- to macro-tidal environments in New Zealand (Hume and Herdendorf, 1988; Hume et al., 2007) and the UK (Pye and Blott, 2014), as well as micro-tidal environments such as South Africa (Cooper, 2001) and Australia (Roy, 1984; Kench, 1999). Hume and Herdendorf (1988) class these environments as a *barrier (beach) enclosed estuary,* which are typically small estuaries with low fluvial inflow, where the inlet is restricted by the barrier beach and direct exchange with the ocean only occurs near high tide (Hume and Herdendorf, 1988; Hume et al., 2007). In the United Kingdom, 25% of

designated bathing beaches feature a river or estuary. Of these 159 beaches, 29, including the present study site, are embayed with an alongshore distance between headlands of less than 3 km, concentrating the dynamic estuarine flows and sediment exchanges over a relatively short length of coast.

Along the world's open coasts, rip currents have been identified as the largest cause of surfzone rescues and fatalities where
35   incident records exist (Scott et al., 2008; Macmahan et al., 2011; Scott et al., 2011; Brighton et al., 2013), causing hundreds of drownings and tens of thousands of rescues globally each year (Castelle et al., 2016). A rip current occurs when water set-up by wave breaking in the surfzone returns back out to sea in a concentrated and often fast-moving offshore flow (Brander, 1999; Macmahan et al., 2006) and has the potential to carry water-users from the shallows out into deeper water. Surfzone circulation typically varies between 'alongshore' flow at the shore which poses a low level of bathing hazard, 'rotational'
40   flow where offshore and onshore currents circulate within the surfzone posing an intermediate level of bathing hazard, and 'exiting' behaviour where rip currents flow directly or obliquely seaward beyond the breaker zone to deeper water, representing the highest hazard to bathers (Scott et al., 2014). However, while studies on bathymetrically controlled rips from various countries have observed rip velocities to average 0.4–1 m/s (Scott et al., 2014; Austin et al., 2010; Macmahan et al., 2010; Mccarroll et al., 2017; Mccarroll et al., 2018), flows within estuary channels on beaches have been observed to
45   average 1–1.5 m/s and exceed 2 m/s during ebbing stages of the tide (Allen, 1971; Lessa and Masselink, 1995; Jiang et al., 2013), with strong seaward flowing circulation. It is therefore surprising that, despite posing an equal or potentially even higher bathing hazard than rip currents, surfzone currents on estuary mouth beaches have received little attention in the scientific literature.

Beach morphology classification schemes identify that intermediate beach states – those featuring three-dimensional
50   nearshore bars and channels – are key locations for rip current activity and bathing hazard (Wright and Short, 1984; Lippmann and Holman, 1990; Masselink and Short, 1993; Scott et al., 2011). While beach classification schemes form the basis of our understanding of surfzone hazards and underpin lifeguard risk assessments in many nations (for example, the UK, Australia, and New Zealand), they ignore the presence of estuary mouths. Where an estuary mouth occurs on a beach, its channel and ebb-tidal delta form an integral part of the beach morphology (Hume et al., 2007) and strongly influence the
55   local flow velocities and nearshore circulation pattern, often promoting offshore flows during the ebb tidal phase (Cooper, 2001; Pye and Blott, 2014; Hume et al., 2007). A better understanding of nearshore circulation patterns and flow velocities at estuary mouth beaches is therefore required to fully understand combined surfzone and estuarine environments and the hazard they pose to bathers.

Figure 1: Examples of estuary mouth beaches from around the world: (a) Mtentu, Eastern Cape, South Africa; (b) Tuross Head, New South Wales, Australia; (c) Crantock, Cornwall, United Kingdom – the study site for this research; (d) Waikawau, Coromandel, New Zealand. © Google Earth Pro.

This contribution aims to investigate the interaction between estuarine flows and surfzone currents on a macrotidal, high-energy beach on the north coast of Cornwall in southwest England and evaluate the contribution of the various interacting processes on surfzone circulation and bathing hazard. A further aim is to develop a predictive system capable of forecasting the level of bathing hazard to forewarn bathers prior to entering the beach. The study site is described in Section 2. In Section 3, a field experiment yielding Eulerian and Lagrangian flow measurements is described, leading to the development of a calibrated and validated hydrodynamic model of the estuary-mouth beach system. In Section 4, the model is used to explore surfzone circulation under various combinations of wave and tide forcing, and their influence on bathing hazard. In Section 5, a bathing hazards forecast system is described that represents the first operational forecast model for bathing hazards on an estuary mouth beach. A discussion and conclusions are provided in Sections 6 and 7.

2 Study site

Crantock beach (Fig. 1c) is located in southwest England on the energetic and macrotidal north coast of Cornwall (Figure 2, upper panel). The beach is flanked on either side by East Pentire and West Pentire headlands, resulting in an embaymentisation ratio (length/depth) of 0.4 (Masselink et al., 2022). Because of the size of the headlands and angle of the beach (310º) relative to the dominant wave approach (280º), the north end of the bay is exposed to more wave energy than the south, resulting in a strong gradient in wave height along the shore; a known precursor for headland boundary circulation

(Castelle and Coco, 2012). Crantock experiences a mean spring tidal range of 6.3 m and is exposed to a mean and 1-year return period significant wave height H_s of 1.5 m and 6.5 m, respectively.

80 Crantock is classed as an intermediate low-tide bar/rip beach following the classification scheme of Scott et al. (2011), but it features distinctly different low tide and high tide morphology. At low tide, the beach face is relatively planar, aside from pronounced boundary rip channels along each headland. At mid to high tide, the morphology is dominated by the ebb tide delta and the channel system associated with the Gannel Estuary. This results in complex three-dimensional features across the upper beach face, comprising often more than one river channel and multiple shoals (Figure 2, middle panel).

85 The Gannel Estuary has a catchment of 41 km² and flows onto Crantock beach at its northeast corner (Figure 2, upper panel) with mean and 5% exceedance riverine flow rates of 0.7 m³/s and 2 m³/s, as measured by a monitoring weir 2 km upstream of the tidal limit of the estuary (https://check-for-flooding.service.gov.uk/station/3135). Tidal discharges into and out of the estuary, however, are an order of magnitude larger than the riverine input (Section 2). For a number of decades, the river channel was artificially pinned against the northern headland by a small rock training wall (Figure 2, middle panel) to

90 maintain a navigation channel across the beach for boats. However, following significant redistribution of the beach sediment during the unprecedented storms of the 2013/14 winter (Hird et al., 2021; Masselink et al., 2016), the river channel avulsed and now meanders laterally across the beach towards the south before discharging seaward through a channel that migrates between the south and north of the bay.

Royal National Lifeboat Institution (RNLI) lifeguards, who provide a lifeguard service at more than 250 UK beaches and

95 have been present at Crantock Beach since 2001, have reported a rapid increase in both beach user numbers and lifeguard rescues in the years since the river avulsed. For example, lifeguard assistance and rescue numbers have increased from < 40 per year in 2014 to > 190 per year in 2018, including two fatalities when lifeguards were not present on the beach. The increase in rescues is likely to be driven in part by the increase in water users at the beach, but lifeguards also report that the river's new position has increased the level of bathing hazard. There is a particular concern that immediately before and after

100 lifeguard patrol hours (10am–6 pm) estuary flows are at their strongest due to the coincidence of high spring tides at these times in the region. Bathers are therefore often exposed to strong ebb-tide flows (Figure 2, lower panel) without any lifeguard supervision. The new river course has carved deep troughs in the beach face which are submerged between mid and high tide, creating steep seabed gradients and spatially and temporally varying flows that are not visible to beach users.
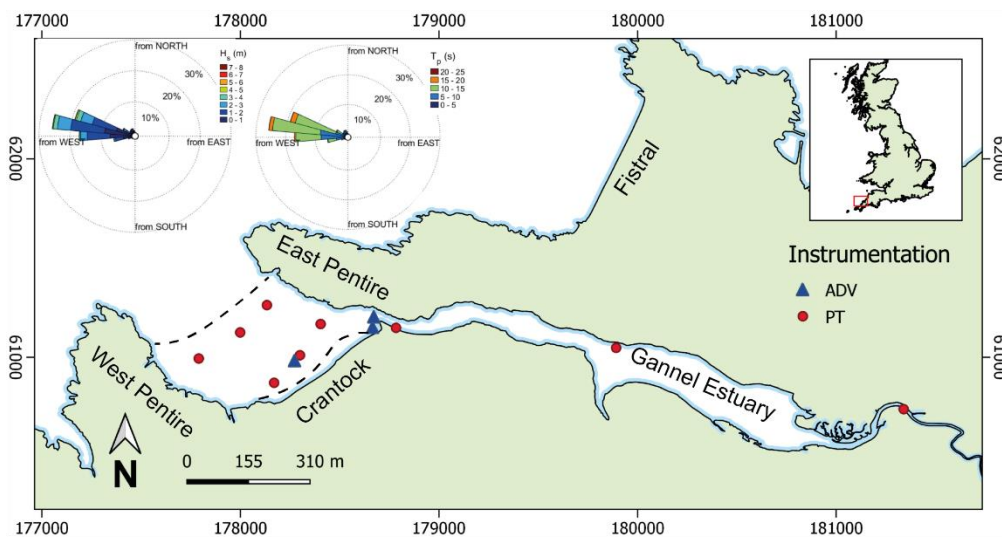
105 **Figure 2: (Upper panel) Crantock Beach and Gannel Estuary, field instrument locations, wave roses, and location in southwest England. Mean low- and high-water lines are shown as dashed lines. (Middle panel) Aerial image showing the river channel across the intertidal beach, relic training wall (yellow rectangle), and former river channel position (yellow dashed line). (Lower panel) Aerial view of river flow during a high ebbing tide, with fixed ADV instrument rigs (yellow circles), and a Lagrangian GNSS drifter (yellow triangle). Note the high level of sediment suspension due to the strong flows.**

110

3 Methodology

3.1 Methodological approach

This study uses a combination of field data and numerical model simulations to investigate surfzone circulation patterns and bathing hazard. The field experiment allowed collection of both Eulerian and Lagrangian flow characteristics under average

115 wave conditions combined with spring tides (Section 3.2) but was limited to the range of wave and tide conditions experienced over the three-day deployment. The numerical model provides the means to understand flow characteristics and bathing hazard under a much wider range of wave and tide conditions (Section 4.4), and with different realisations of the beach morphology (Section 4.5). Furthermore, the model provides the ability to 'switch off' the estuarine flows (Section 4.6) enabling us to disentangle the contribution of wave and estuary driven hydrodynamics on the surfzone circulation.

120 ### 3.2 Field data

The field experiment (11th - 14th May 2021) focussed on the collection of topographic and bathymetric survey data, Eulerian wave and current measurements, and Lagrangian flow observations. Topographic data were collected using high-resolution aerial imagery captured with a DJI Phantom 4 RTK uncrewed aerial vehicle (UAV), equipped with accurate GNSS positioning system, flown across the site collecting multiple aerial images with an 80% overlap. The images were processed

125 using photogrammetric techniques (structure-from-motion and multiview stereo) to create a digital elevation model (DEM) of the site. The DEM achieves a vertical RMSE of 0.03 m compared to spot checks against ground control points. The UAV flights were conducted around low water to maximise the coverage and visibility of the river channels. Once the data was captured, it was processed and translated onto a regular grid for further analysis.

For the full model domain to be mapped, a bathymetric survey was conducted at high tide to map the subtidal region, as well

130 as overlap with the intertidal areas covered by the UAV. Multiple cross-shore transects ~25 m apart were recorded using a Valeport Midas Surveyor echosounder (acoustic frequency 210 kHz; sample rate 6 Hz), pole-mounted on an inflatable surf rescue vessel, with external Trimble RTK-GNSS positioning (Trimble 5800; sample rate 1 Hz). The bathymetric survey achieves a vertical RMSE of 0.1 m. By merging the echosounder and UAV datasets the full survey region was extended down to ~10 m water depth, covering the full embayment (Fig. 1).

135 Eulerian measurements were collected by three Nortek Acoustic Doppler Velocimeters (ADVs) deployed on a rigid frame to allow current measurements to be logged ~0.1 m above the beach (Figure 2 and Figure 3), measuring alongshore, cross-shore

and vertical flow velocities. Wave and tidal signals were logged using an array of nine pressure transducers (PTs) installed at bed level across the survey domain, three of which were co-located with ADVs (Fig. 2). All sensors were programmed to log at 4 Hz continuously. Outliers and spikes in the datasets were removed as part of quality control checks.

140   Lagrangian measurements were collected using GNSS-tracked surfzone drifters (Figure 3), which were telemetered in real-time allowing shore based logging using QPS Qinsy software package (following Mouragues et al., 2020). Six drifters were deployed at numerous locations multiple times across the survey area throughout the tidal cycle. The drifters both transmit and log their position as they follow the surface currents. The raw data was then processed to remove time periods when the drifters were stationary on the beach, being deployed by hand or being recovered by the inshore survey boat. The cleaned

145   data provides an x, y, t dataset where t = time.
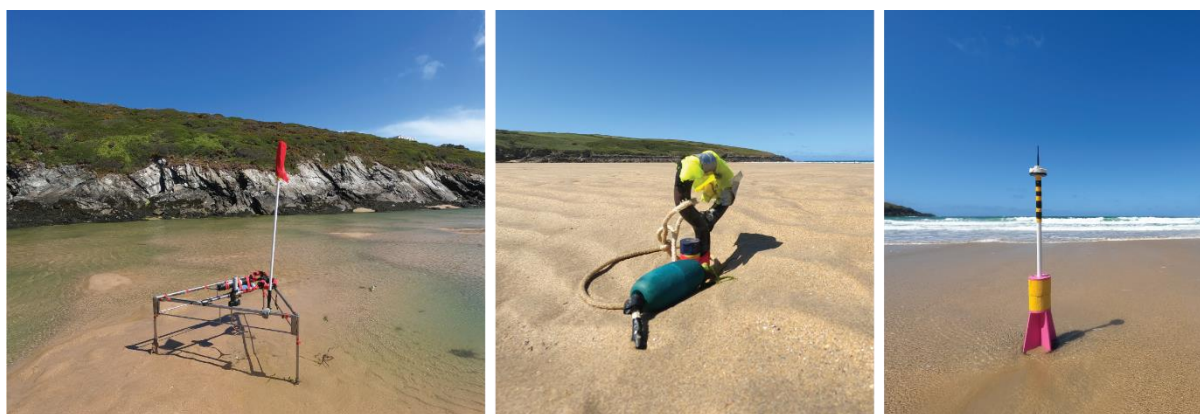
Figure 3: Field instrumentation. (Left panel) Frame supporting the ADV logger, batteries, and sensor head ~0.1 m above the bed; (middle panel) pressure transducer sensor installed at bed level using a sand screw; and (right panel) a Lagrangian 'GNSS drifter' designed to map surface currents.

150
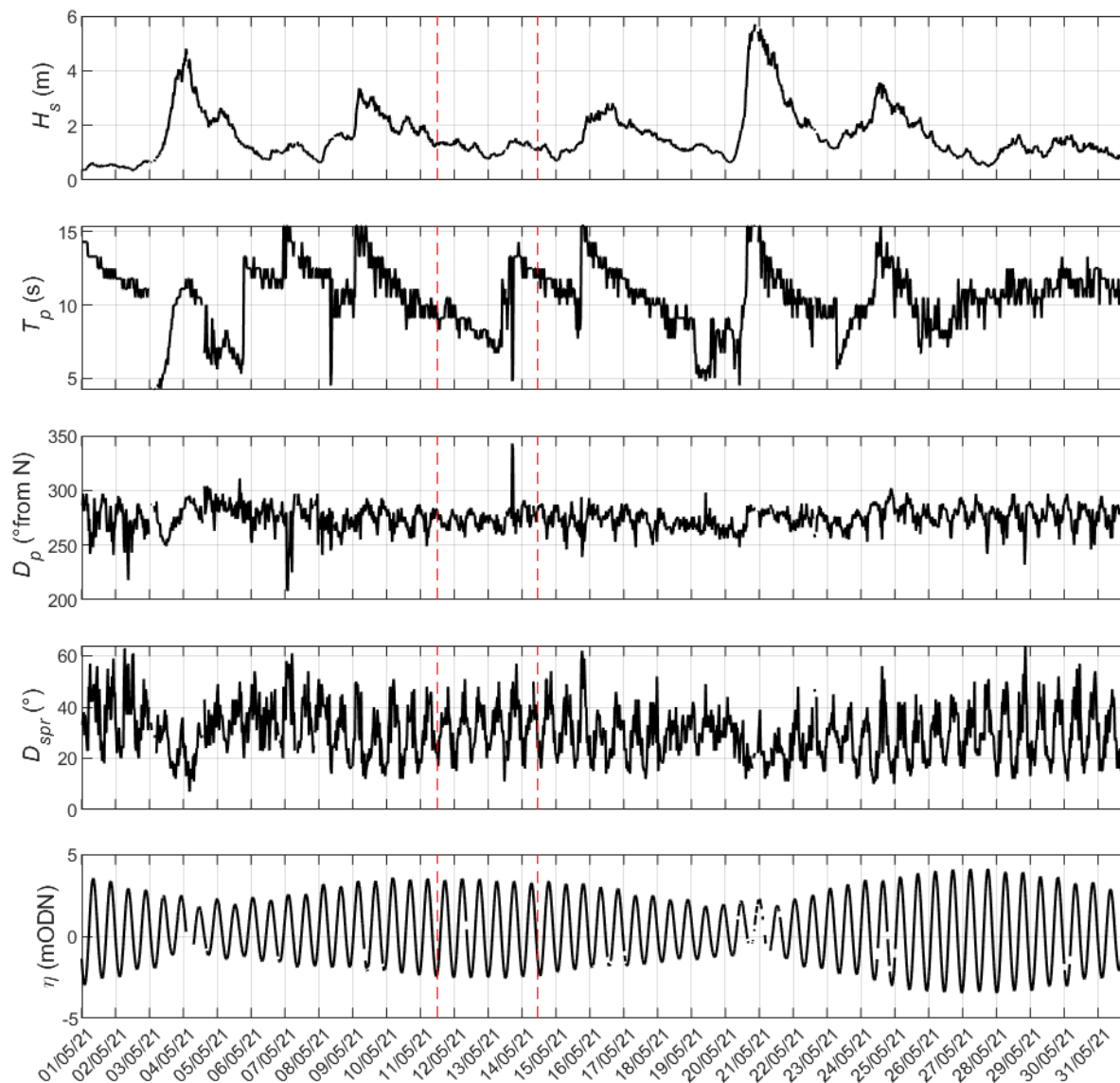
Figure 4: Hydrodynamic conditions during the field deployment period (red dashed lines) measured at a waverider buoy 7 km south of Crantock and a tide gauge 29 km north of Crantock (https://coastalmonitoring.org/cco/). From top to bottom: significant wave height, H_s; peak wave period, T_p; direction of wave approach D_p; wave directional spread D_{spr}; and tidal water level, η.

3.3 Numerical model

The process-based numerical model XBeach was used to simulate rip current and estuary-driven flows across Crantock beach. The model solves for the time-dependent short wave action-balance equations, roller energy equations, the non-linear shallow water equations of mass and momentum, sediment transport formulations, and morphological updating (Roelvink et

al., 2010). Wave group dissipation is modelled (Roelvink, 1993; Daly et al., 2012), and a roller model (Svendsen, 1984; Nairn et al., 1991; Roelvink and Reniers, 2011) is used to represent the momentum carried after wave breaking. Radiation
165   stress gradients (Longuet-Higgins and Stewart, 1962, 1964) then drive infragravity motion and unsteady currents in the model, which are solved with the non-linear shallow water equations (Phillips, 1977). In the 'surf beat' mode of operation used in this study, XBeach solves the variation of the short-wave envelope on the scale of individual wave groups (Roelvink et al., 2018), which has previously been found to reproduce measured hydrodynamics at dissipative and intermediate beaches favourably, including channel and boundary rip current behaviour (Austin et al., 2013; Scott et al., 2016; Mccarroll et al.,
170   2015; Dudkowska et al., 2020; Mouragues et al., 2021). In the present study, morphological updating was switched off.

3.4 Model domain

A 2D-H (two horizontal dimensions, depth averaged) model was developed covering the full extent of Crantock beach (Figure 5), from the supratidal down to a seaward depth of 20 m below Ordnance Datum Newlyn (ODN). The domain was developed using the survey data described in Section 3.2 to cover the intertidal (-1 to +5 m ODN) and sub-tidal (-10 to +1 m
175   ODN) regions, respectively. Repeat surveys were conducted in May 2021, August 2021, May 2022, and July 2022, providing four different realisations of the beach and estuary mouth morphology (Section 4.6). These data were complimented by open-source aerial LiDAR data, surveyed in February 2019, and single beam bathymetry data, surveyed in 2007, by the regional coastal monitoring programme (https://coastalmonitoring.org/) to cover the estuary and supratidal areas, as well as offshore subtidal (-10 to -20 m ODN) region, respectively. Prior to developing the model domain, the various
180   spatial data types were merged into a single 1 m x 1 m gridded spatial data set using two-dimensional linear interpolation, while ensuring that smooth elevation transitions were achieved between the different data types.

To optimise computational effort, the model grid was developed with a variable resolution. Within the embayment, the cross-shore and alongshore resolution was fixed at 4 m, while outside the bay the cross-shore resolution was gradually decreased from 10 m depth using the Courant condition to optimise resolution based on water depth, giving a cross-shore
185   resolution of 34 m at the offshore model boundary. Either side of the bounding headlands, the alongshore resolution was decreased from 4 m to a maximum of 20 m at the lateral boundaries. The model extends linearly 200 m to the northeast and 400 m to the southwest of the bounding headlands to ensure that any wave shadowing from the lateral boundaries does not impact conditions within the bay, and a linear transition was implemented at the offshore boundary to remove any near-boundary   gradients   (Figure   5a).

190
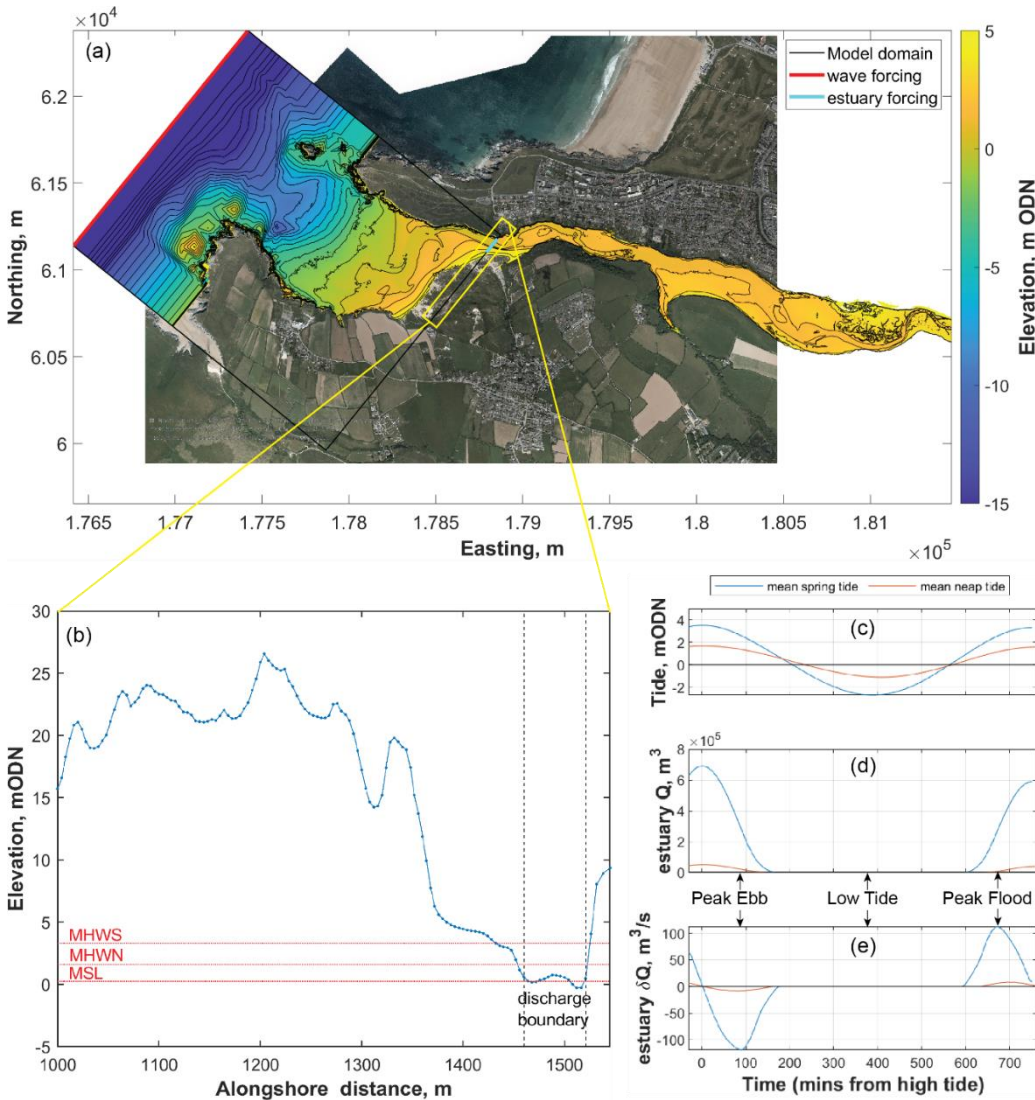
Figure 5: (a) Model domain (black box) overlaid onto aerial imagery of Crantock Beach and surrounding area. The coloured topography shows the elevation of beach and estuary morphology. (b) Alongshore cross section of the model DEM (blue dotted line) in the area where the Gannel enters Crantock beach, showing the location (black dashed lines) and resolution (blue dots) of

195 **the discharge forcing boundary. Hypsometry of the Gannel estuary, including mean spring and neap tidal excursion (c), submerged volume, Q (d), and change in volume δQ (e) of the estuary. Aerial imagery courtesy of National Network of Regional Coastal Monitoring Programmes of England, © 2024 NNRCMP.**

3.5 Boundary forcing conditions

200   The XBeach model was forced with waves uniformly along the seaward boundary, while tidal variation was imposed uniformly on all four corners of the modal domain. For calibration and validation, wave forcing was obtained from a nearby directional waverider buoy located 7.5 km southwest of Crantock Beach in 10 m water depth at mid-tide (https://coastalmonitoring.org/), with waves reverse shoaled to the boundary depth of 20 m using linear wave theory. Tidal variation was obtained from Admiralty tide charts. Once the model was calibrated (Section 3.7), seventy-two combinations

205   of wave and tide conditions were run in the model covering wave heights of 0.5–3 m, wave periods of 6–12 s, and wave approaches from 269°–304°, with each set of wave conditions run over a mean neap tidal cycle and a mean spring tidal cycle (with 30 minutes spin up time). Each 13-hour simulation was then divided into 1-hour tidal segments, providing 6,084 unique combinations of wave and tide forcing from which to evaluate circulation patterns and bathing hazard from the simulated flow fields.

210   The XBeach model itself does not include the Gannel estuary, as, while it is possible to compute estuary flows within XBeach (Hartanto et al., 2011), this would add considerable computational effort given the spatial extent of the estuary. Instead, the ebbing and flooding flows from the Gannel were imposed using a discharge boundary. This forces a flow of water into the model domain (positive discharge) or out of the model domain (negative discharge) to describe the ebbing and flooding of the tide, respectively, through the relatively narrow estuary mouth at the north-eastern side of the beach.

215   Discharges were applied to the model across a 60-m section of the landward model boundary, covering the deepest part of the river channel (Figure 5b).

The submerged volume of the Gannel estuary (Q; Figure 5d) was quantified landward of the model boundary beneath a range of tidal elevations (Figure 5c), through interrogation of the Gannel Estuary DEM (Figure 5a). The difference in volume between two elevation plains (dQ), and the timeframe over which the tide changes between those elevations (dt),

220   were then used to estimate the tidal discharge into or out of the estuary at different stages of the tide (dQ/dt). This analysis indicates peak discharges are 8 m^3/s and 110 m^3/s during average neap and spring tides, respectively (Figure 5e). For the scenario simulations, the discharge applied at the boundary was computed from the estimated spring and neap tidal discharge rate at a given point in time, plus an additional 2 m^3/s to conservatively account for fluvial flow (Section 2).

3.6 Quantification of flow behaviour and bathing hazard

225   To assess surfzone circulation and quantify bathing hazard, Generalised Lagrangian Mean flow velocity (Groeneweg and Klopman, 1998) fields from XBeach were used to advect virtual drifters within the model and the drifter tracks were then analysed to provide bathing hazard proxies. The drifters were seeded within the surfzone randomly in time and space, seeding across a depth range representing safe-depth limits for children to adults (0.7–1.2 m, respectively), informed by previous studies (Mccarroll et al., 2014b; Mccarroll et al., 2015). 1,500 drifters were seeded during each simulated period,

with 500 of these seeded along the bank of the River Gannel where the estuary enters the beach and the rest seeded along the shoreline of the beach. Each virtual drifter was advected for 20 minutes, or until they had returned to a safe water depth (< 0.7 m).

Seaward Lagrangian flow speed U_{off} and the percentage of drifters exiting beyond the extent of the surfzone E have previously been shown to provide good predictors of bathing hazard (Austin et al., 2013; Scott et al., 2014). We applied these parameters to the virtual drifter data from XBeach to quantify when and where peak bathing hazard occurs. Low values of both U_{off} and E represent the lowest bathing hazard, as bathers would be advected slowly and retained in shallow water, while high values of U_{off} and E represent the highest hazard as bathers would be transported quickly towards deep water. Other combinations represent a medium hazard level.

Defining and determining a single value of U_{off} and E for each simulation is not trivial (Castelle et al., 2010; Austin et al., 2013), as surfzone velocities and circulation vary spatially and temporally. In rip current studies, U_{off} (often termed U_{rip}) is usually quantified at a pre-defined location such as the rip channel neck under study (Austin et al., 2013; Castelle et al., 2010), and E similarly requires a specific cross-shore threshold to be crossed in order to count surfzone exits. In the present study we define U_{off} following the approach of Austin et al. (2013) using hourly-averaged Lagrangian velocities from independent drifter passes through 10 m spatial bins:

$$U_{off} = \sqrt{\overline{u_{off}^2} + \overline{v^2}} \tag{1}$$

where U_{off} is the offshore-directed flow velocity, v is the alongshore-directed velocity, and the overbar signifies time averaging. The reader is referred to Castelle et al. (2010) for the method of determining independent drifter passes. Only spatial bins with at least five independent drifter passes were included, and the spatial bin with the maximum U_{off} value defines U_{off} for the entire beach. The U_{off} values presented herein therefore represent a spatial maximum, akin to U_{rip} values from previous rip current studies. To quantify the proportion of surfzone exits E occurring during each 1-hour simulated period, we determine the percentage of virtual drifters that travel seaward at least the same distance as the alongshore-averaged surfzone width. For comparability with previous studies, we define the seaward extent of the surfzone as the location where the cross-shore roller energy exceeds 10% of its cross-shore maximum (Reniers et al., 2009), determining the average width of the surfzone across the length of the embayment.

3.7 Model calibration and validation

The developed XBeach model was calibrated against the first tidal cycle of Eulerian field data (Figure 6 and Figure 7), with measured and modelled wave height compared at each of the surfzone PTs, and flow velocity compared at each of the three ADV locations. Six hydrodynamic tuning parameters were adjusted in the model during calibration: the wave breaking formulation, the breaker slope coefficient, the wave dissipation coefficient, the wave breaker parameter, the bed friction formulation, and the bed friction coefficient. The wave and flow comparison was found to be insensitive to the breaker formulation, breaker slope coefficient, and wave dissipation coefficient, so these parameters were left at their default values.

The wave breaker parameter γ, which controls the break point and surfzone width, and the bed friction formulation and coefficient C, which influence the current velocities, had a greater effect on the hydrodynamic performance of the model. Optimal settings for these parameters were found to be a breaker coefficient of $\gamma = 0.50$ and a Chezy bed friction coefficient

265   of $C = 45\ \text{m}^{1/2}/\text{s}$.

Another important calibration for the present study is the weighting of the discharge during the flooding and ebbing stages of the tide, applied at the estuarine boundary. Initially it was assumed that *dQ/dt* could be applied directly from the hypsometric analysis (Section 3.5); while this was found to replicate flow velocities on the ebbing tide well, it overpredicted landward flow velocities on the flooding tide. Peak ebb tide velocities have been observed at other sites to occur in the deepest

270   morphological channels, while peak flood tide velocities are generally weaker and do not necessarily occur in the deepest channels (Allen, 1971; Lessa and Masselink, 1995). A weighting coefficient is therefore required to account for the fact that while the ebb tide exits directly through the river channel (here used as the discharge boundary), the flood tide enters the estuary through both the channel and the surrounding shoal/beach areas. Applying *dQ/dt* across our fixed discharge boundary location (Figure 5) is therefore a reasonable representation during the ebbing phase of the tide, but not during the

275   flood phase. To account for this, we use separate discharge coefficients, α, for the flood tide (α_{flood}) and ebb tide (α_{ebb}) periods, applied to the hypsometric discharges as:

$$(\text{dQ/dt})\ \alpha_{flood} \qquad \text{for } \frac{dQ}{dt} \geq 0 \tag{2}$$

$$(\text{dQ/dt})\ \alpha_{ebb} \qquad \text{for } \frac{dQ}{dt} < 0 \tag{3}$$

Optimal values to replicate the estuary flow velocities were found to be $\alpha_{flood} = 0.5$ and $\alpha_{ebb} = 1$. However, this may not

280   be generalisable and would need to be calibrated for other study sites.

Using these calibration settings, the model was validated against the Eulerian data from the entire field deployment period (three tidal cycles). Model skill was quantified using the Root Mean Square Error (RMSE), defined as:

$$RMSE = \sqrt{\frac{1}{n}\sum_{i=1}^{n}\left(X_{XB(i)} - X_{M(i)}\right)^2} \tag{4}$$

where X refers to the hydrodynamic variable being assessed, and subscripts *XB* and *M* refer to the modelled and measured

285   values, respectively. The RMSE values were also normalised (NRMSE) by the mean H_s value or maximum U value at each instrument location across the periods under comparison to assess the relative magnitude of the error (Mouragues et al., 2021).

4 Results

4.1 Eulerian and Lagrangian field measurements

290   The field experiment was conducted during approximately average summer wave and tide conditions ($H_s = 0.7$–1.4 m, $T_p = 7$–14 s, $D_p = 260$–290°, tide range = 5.6 m; Figure 4). Water level data from the mid-estuary PT shows that the estuary began

to fill as the tide increased above ~1 mODN, with the volume peaking at approximately 500,000 m³ at high tide (Figure 6). Estuary flow, however, peaked just over an hour before high tide (landward discharge) and after high tide (seaward discharge), with fluxes of up to 100 m³/s estimated from the water levels measured during the experiment (Section 3.2).

295 The estuary discharge generated strong surfzone flows, which can be seen in the observed field data. Figure 6 demonstrates Eulerian velocities from the ADVs located on the intertidal ebb shoal bank adjacent to the estuary mouth, and within the estuary mouth itself. Peak velocities in the estuary mouth occurred 1–2 hours before and after high tide and diminished to zero at high tide. Comparable velocities were measured on the ebb shoal bank, 30 minutes after (before) the estuary mouth on the rising (falling) tide. The seaward flow out of the estuary measured on the falling tide was 1.5–2 times faster than the

300 landward flow on the rising stage of the tide, with seaward velocities at the ADV peaking at 0.75–1 m/s and landward velocities at 0.5 m/s for these two example tides. However, as the ADV in the estuary mouth was not in the deepest part of the channel, it is expected that peak flows exceeded 1 m/s elsewhere.

The intertidal beach face ADV shows velocities remained notably low on the rising and high stages of the tide but increased rapidly up to 1.5 m/s on the falling tide especially once the water level had dropped below 1.5 mODN, concentrating the

305 flow within the submerged beach face river channels. This ADV was located in the centre of the channel, so this represents a realistic estimate of the peak ebb tide velocity. The *u* and *v* velocity components (Figure 7) indicate that cross-shore flows dominated within the seaward-facing estuary mouth, while alongshore flows dominated on the ebb-shoal bank and within the alongshore-oriented beach face river channel.
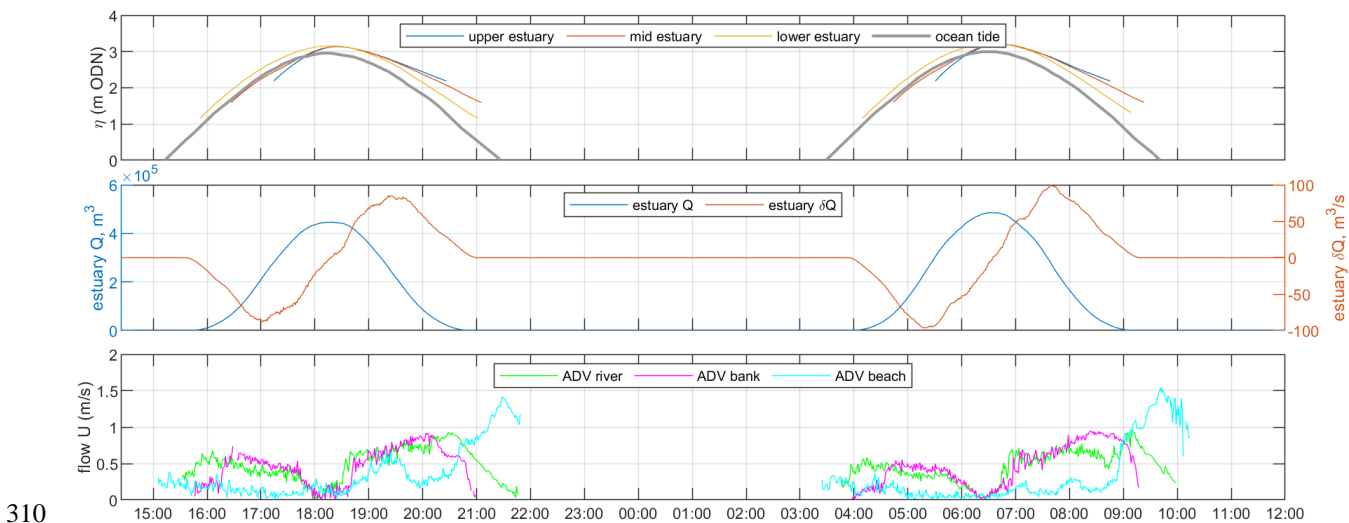
310

Figure 6: Eulerian field data collected in the vicinity of the Gannel estuary over the first two high tides of the field experiment. Upper panel: water level signal measured by PTs at different locations in the Gannel estuary and ocean tide level from Admiralty Tide Charts. Middle panel: Gannel estuary volume, *Q*, and change in volume, *dQ*, estimated from the mid estuary PT data, as per Section 3.5. Lower panel: velocity magnitude measured by ADVs in the estuary mouth ('ADV river'), ebb shoal river bank ('ADV

315 **bank'), and within the beach face channel (ADV beach). See for instrument locations. Note that the estuary is dry 3 hours either side of low tide.**

The Lagrangian GNSS drifter tracks reveal that various circulation behaviours occurred simultaneously across the beach, including alongshore, rotational, and exiting flows, creating a complex flow field (Figure 8). The observed circulation
320   patterns evolved from low to high tide due to differences in the underlying beach morphology, as well as the activation and de-activation of the estuary at mid-tide. The GNSS drifters show a strong estuarine current flowing seaward during the ebbing high tide (Figure 8, lower panel), which diverts laterally across the beach through various submerged river channels. Median Lagrangian velocity observed during this phase of the tide was 0.5 m/s, but drifter velocities exceeding 1 m/s occurred where the river channel bends sharply away from the northern headland. Although many of the GNSS drifters
325   exited the surfzone during the ebbing phase of the high tide, rotational flow also returned some drifters shoreward and back along the shore towards the main river channel (Figure 8). Conversely, at low tide the GNSS drifters show weaker onshore and alongshore flows leading to boundary rips at either headland, which exit seaward or circulate back towards shore (Figure 8, upper panel). Median Lagrangian velocity during this phase of the tide was 0.3 m/s, with peak velocities exceeding 0.6 m/s within the surfzone and in the neck of the boundary rip channels. Apart from a shallow (< 1 m), fast flowing fluvial
330   component, the estuary was inactive at tide levels below ~0 mODN.

4.2 Comparison of modelled and measured flows

Comparing the measured and modelled Eulerian flows (Figure 7), the XBeach model reproduces the flow magnitude and phase from the ADVs well, albeit with some underprediction of flow during the ebbing tide on the ebb-shoal bank and within the alongshore-oriented beach face river channel. The model reproduced the direction of the Eulerian flows well, with
335   cross-shore velocities dominating in the river channel, and alongshore velocities dominating on the ebb-shoal riverbank and in the alongshore-oriented beach-face river channel. Overall, the calibrated model achieved RMSE (NRMSE) of 0.2 m (20%) for H_s, 0.16 m/s (20%) for u velocity, and 0.22 m/s (21%) for v velocity.
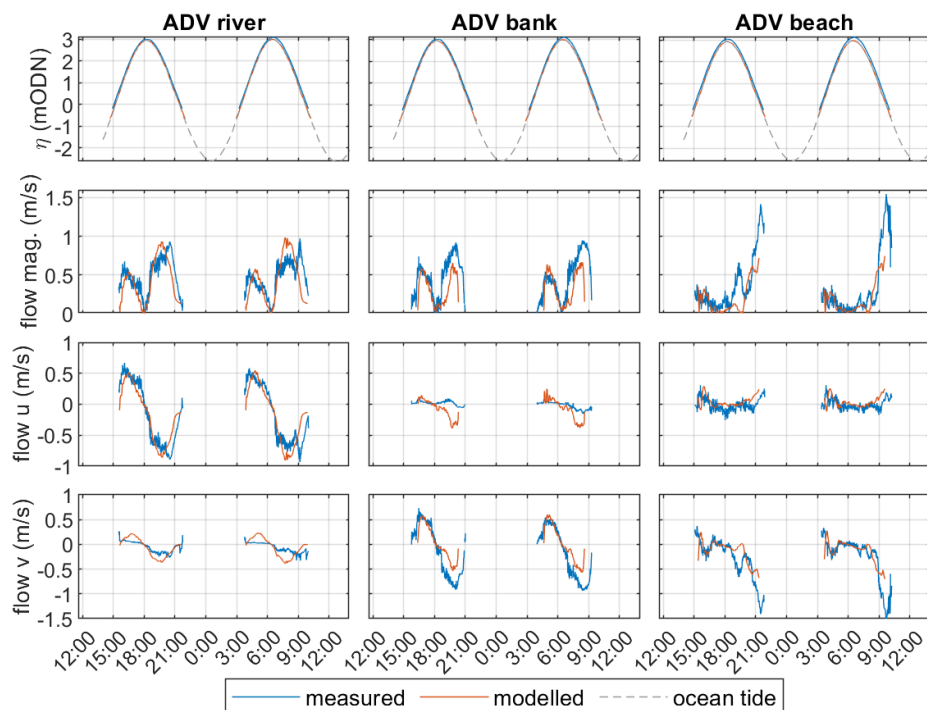
Figure 7: Comparison between measured and modelled flow velocity at the three Acoustic Doppler Velocimeters (ADV) during the
340 **first two tidal cycles of the field experiment used for model calibration. The location of each ADV is shown in Figure 2. Positive**
(negative) *u* velocities represent landward (seaward) flows, while positive (negative) *v* velocities represent northward (southward)
flows.

Compared to the Lagrangian circulation patterns measured in the field during the low tide period (Figure 8, upper panels),
the bin-averaged velocities from the virtual drifters (Section 3.6) reproduce the measured boundary rip velocities at the north

345 and south headlands (~0.5 and ~1 m/s at the southern and northern headlands, respectively). The virtual drifters also capture
the net onshore flow in the middle of the bay and net seaward flows in the southern half of the bay and adjacent to the north
headland. During the high ebb-tide period (Figure 8, lower panels), both the measured and modelled drifters coherently
follow the river channels in the beach face, with flows diverting away from the north headland across the beach before either
exiting seaward through the beach face river channel, or circulating back towards the estuary along the shore. The model

350 reproduces the strong seaward ebb-tide flow entering the beach from the estuary, where median Lagrangian velocities
exceeding 1 m/s were both modelled and observed. The circulation patterns show that the ebb-tide flows convey water
rapidly through the main river channel before they connect to channel rips and boundary rips 100's of meters away from the
estuary mouth.

Overall, the calibrated model reproduces the measured Eulerian and Lagrangian flows from the three-day field deployment

355 well, especially considering the complexity of the flow field, and is therefore deemed suitable to assess surfzone circulation
under a wider range of conditions.
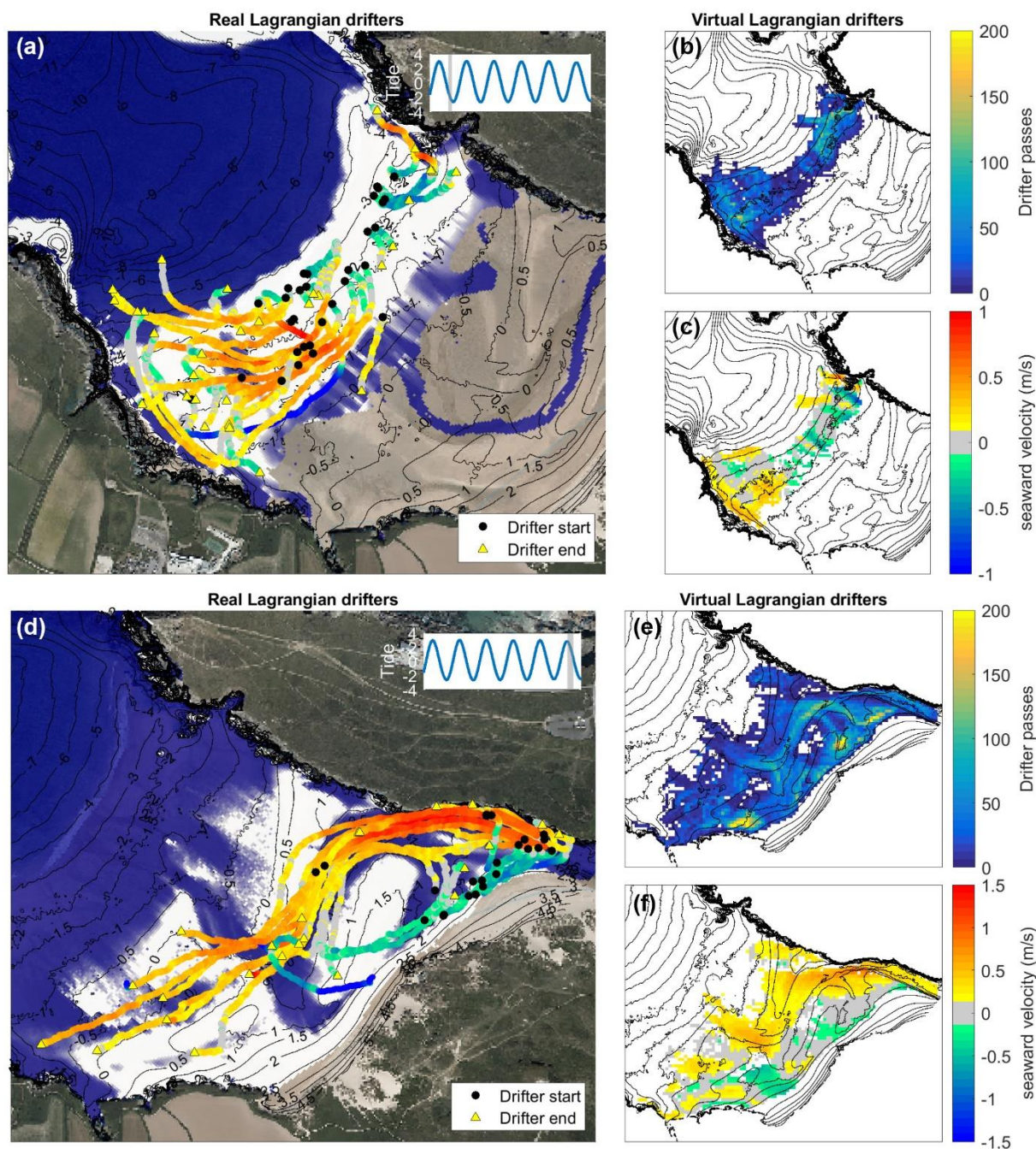
Figure 8: Comparison of measured and modelled circulation patterns using Lagrangian velocities from real GNSS drifters (panels a and d), and virtual drifters seeded in the XBeach model (panels b, c, e, f) averaged onto a 10-m spatial grid. Panels a–c show low tide drifter data from the 12th of May 2021 and panels d–f show high ebb-tide drifter data from the 14th of May 2021. Blue and

white areas in the left panels show average water level and predicted wave dissipation > 1 W/m² during the field experiment, for reference. Aerial imagery courtesy of National Network of Regional Coastal Monitoring Programmes of England, © 2024 NNRCMP.

4.3 Simulated Lagrangian circulation

In the following sections, the calibrated XBeach model is used to explore circulation patterns under a wider range of wave and tide conditions than was achieved in the field, as well as quantifying the exit potential and flow velocities under different forcing scenarios.

4.4 Influence of tidal stage and wave energy

The XBeach simulations demonstrate that tidal translation across the beach significantly alters the surfzone circulation. Different circulation patterns and associated bathing hazard are seen at high, mid, and low tide, and, furthermore, circulation is predicted to be distinctly different under a rising tide or a falling tide. For example, during a high ebbing spring tide with average waves (Figure 9a), the virtual Lagrangian drifters are carried alongshore by littoral currents before exiting seaward in a narrow and fast flowing estuarine current (U_{off} = 1.1 m/s; E = 56%). At mid-high tide stages (Figure 9b, c, f, g), the surfzone is wide and the flows become channel-constrained. The flows follow the path of the submerged river channels alongshore and seaward towards channel rips and headland boundary rips, which are enhanced when the tide is ebbing (U_{off} = 1.2 m/s; E = 25%) and diminished, but still present, when the estuary is flooding (U_{off} = 0.52 m/s; E = 0%). Below mid-tide (Figure 9d, e), the river channels and estuary discharge no longer influence surfzone circulation, and seaward flows predominantly occur within headland boundary rips at either side of the beach (U_{off} = 0.59 m/s; E = 13%).

Tide range influences the hazard signature in two distinct ways. Firstly, it determines how much water is flushed from the estuary during the ebbing high tide phase, with an order of magnitude more estuary discharge (Figure 5) during a spring tide (Q ≈ 700 m³) than during a neap tide (Q ≈ 50 m³), which substantially increases the estuary-driven flows in the hour following high spring tide (U_{off} = 1.1 m/s; E = 56%) compared to those following high neap tide (U_{off} = 0.63 m/s; E = 15%). However, at equivalent tide levels, the circulation patterns are almost identical during a neap and spring tide (not shown here) because the ebb shoal channels dictate the circulation. Secondly, during high (Figure 9a) and low (Figure 9e) spring tides, the beach gradient is steeper and the surfzone is narrower than at any stage of a neap tide. This controls the ability of estuary and rip current flows to exit the surfzone, with a far wider, more saturated surfzone, and subsequently fewer exits, occurring during a neap tide than under high or low spring tides.

Figure 10 summarises the predicted flow velocity and exit potential under various combinations of wave and tide conditions. Wave power is parameterised relative to the timeseries mean using a 'wave factor' parameter (Scott et al., 2014) $W_f = H_sT_P/\overline{H_sT_P}$, which describes the ratio between the associated H_sT_P (proportionally representing wave power) and the 16-year summer (June, July, August) mean ($\overline{H_sT_P}$). This analysis shows that below mid-tide, tidal stage and direction become

395   relatively unimportant, but seaward flow and exit potential are predicted to increase with increasing wave power, from $U_{off} =$
0.3–0.5 m/s and $E = 5$–15% when $W_f < 0.5$, to $U_{off} = 0.5$–0.7 m/s and $E = 10$–25% when $W_f \approx 0.5$. At $W_f = 3$–4, U_{off} is 0.7–
1.0 m/s and E is 20–40%. However, above mid-tide there are significant differences predicted in flow velocity and exit
potential at different stages of the tide. The least hazardous conditions are predicted to occur during a rising mid to high tide
(Figure 10, left panel) with wave power below average, when seaward flows are almost entirely absent ($U_{off} < 0.5$ m/s; $E =$

400   0%). Conversely, the most hazardous flows are predicted to occur during ebbing high spring tides (Figure 10, right panel)
with wave power below average ($U_{off} = 1.5$ m/s; $E = 58\%$), when the estuary discharge can flow seaward completely
unhindered by the surfzone. As wave power increases above average ($W_f > 1$), these ebbing flow velocities are predicted to
remain high, but exit potential decreases significantly, as estuary flow is hindered by a wider, more saturated surfzone.

405
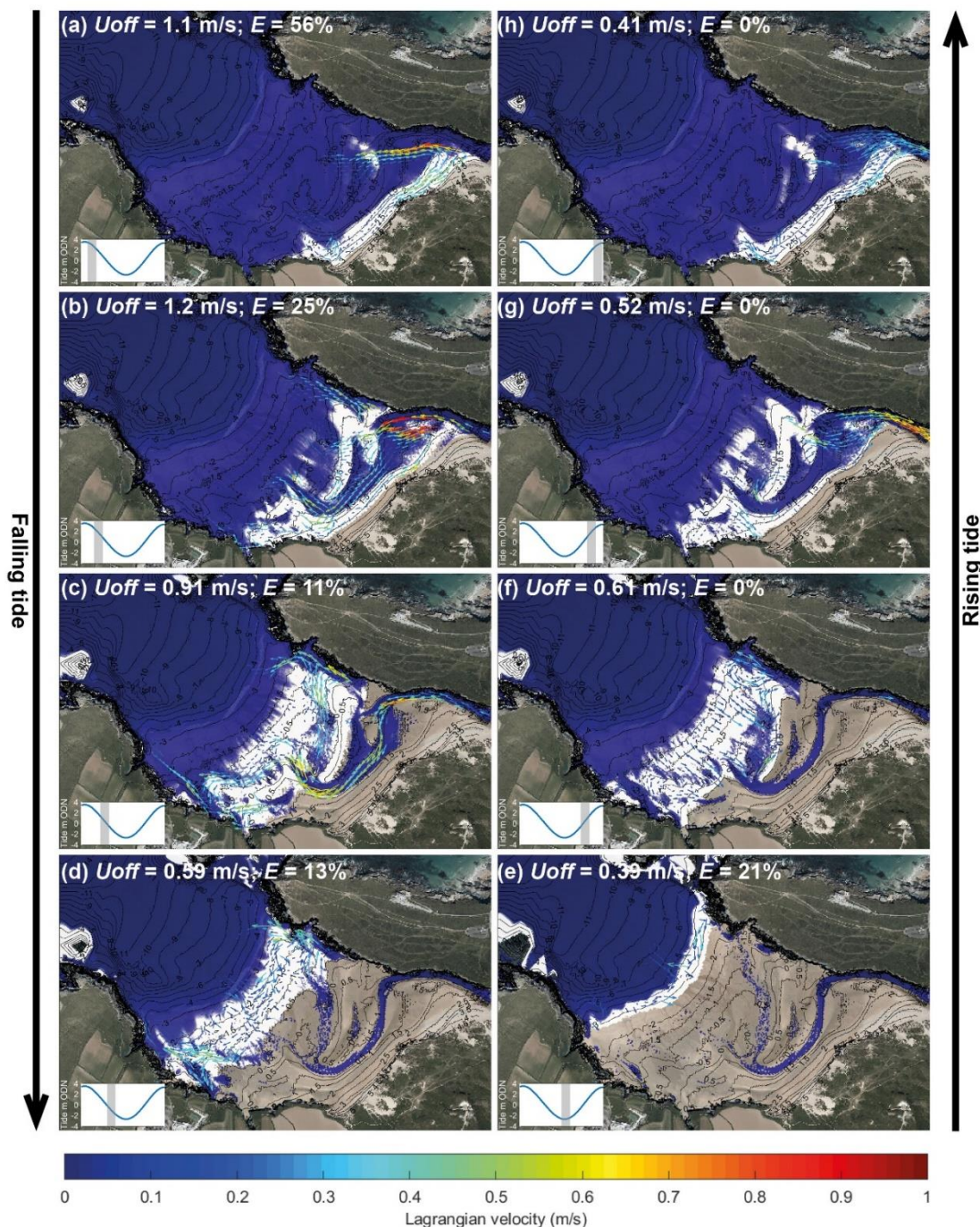
Figure 9: Simulated Lagrangian surfzone circulation from XBeach over a spring tidal cycle combined with average wave conditions ($H_s = 1$ m, $T_p = 12$ s, $D_p = 279°$). Vectors represent virtual drifter tracks averaged over 1 hour onto 10 m spatial bins (every other bin shown for clarity). The 10 m spatial bin with the maximum seaward directed flow velocity defines U_{off} for the entire beach, while E is computed from the proportion of virtual drifters that exit the surfzone (Section 3.6). Contours indicate beach morphology (m ODN) while filled areas show submerged regions (blue) and breaker dissipation (white). Tidal stage is

shown in the inset panels. Aerial imagery courtesy of National Network of Regional Coastal Monitoring Programmes of England, © 2024 NNRCMP.

415

Figure 10: Proportion of surfzone exits (*E*, bubble size) and offshore-directed drifter velocity (*U_off* m/s, bubble colour) from XBeach simulations with a mean spring tide and mean angle of wave approach. Bubble size range represents $0 \leq E \leq 58\%$. Results are plotted as a function of water level η and wave factor $H_s T_P / \overline{H_s T_P}$. The vertical dashed line indicates average wave power ($\overline{H_s T_P}$), while the horizontal lines represent Mean High Water Spring (MHWS), Mean High Water Neap (MHWN), Mean Sea Level (MSL), Mean Low Water Neap (MLWN), and Mean Low Water Spring (MLWS) water levels.

420

4.5 Influence of estuary discharge

The estuary has been shown to drive extremely strong seaward flows through the surfzone in the hours following a high

425   spring tide, with flow velocities up to 1.5 m/s. However, the estuary influences the flow dynamics in two distinct ways: (1) water flushing into and out of the estuary drives increasingly strong surfzone currents as tide range increases; and (2) the river channel morphology acts to constrain surfzone flows in the same way that rip channels funnel wave-driven flows. In fact, ignoring estuary flows, the ebb shoal delta acts very much like a bar-rip system found on an intermediate morphology beach, providing shallow areas that induce wave breaking and deeper areas where wave-driven flows can return seaward. To

430   demonstrate this, XBeach simulations were compared with and without estuary discharge activated in the model, to
disentangle the effect of the river channel morphology from the strong estuary flows (Figure 11).

In the hours immediately prior to a high spring tide a significant flow of water floods the estuary (Figure 11a), with strong
landward flows occurring near the shore adjacent to the estuary. With estuary discharge switched off in the model (Figure
11b), strong flows are still predicted to occur at the shore due to the oblique angle of the shore to the breaking waves, but the
435   strong landward flows in the river channel no longer occur. However, wave breaking on the ebb shoal delta is predicted to
drive weak seaward flowing rips in the river channel away from the estuary, whether estuary discharge is switched on or off,
indicating that the river channel morphology induces channel rip behaviour independently of the estuary flows.

Immediately following a high spring tide there is a strong seaward flow driven by the estuary (Figure 11c). Switching the
estuary discharge off in the model (Figure 11d) unsurprisingly has a strong effect on the flows immediately adjacent to the
440   estuary mouth, but in the river channels more than 300 m from the estuary mouth the predicted circulation patterns are very
similar whether estuary discharge is applied in the model or not. The river morphology is predicted to induce channel rip
behaviour and contributes to bathing hazard independently from the estuary flows. Seaward flows in the main river channel
in the middle of the beach are predicted to be similar in magnitude ($U_{off} = 0.6$ m/s) in the absence of estuary flows, to those
with estuary flows activated ($U_{off} = 0.8$ m/s), as are the slightly stronger boundary rip current velocities ($U_{off} = 1$ m/s).

445
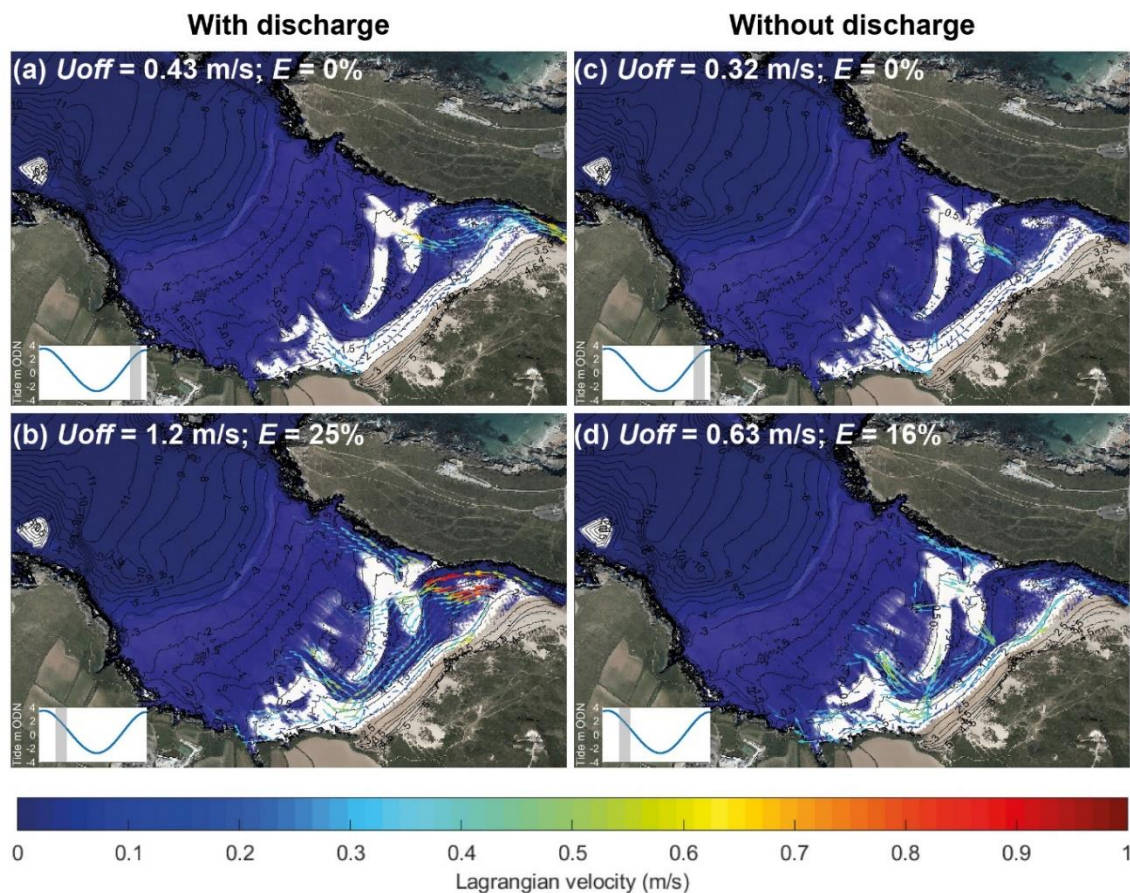
Figure 11: Simulated Lagrangian surfzone circulation from XBeach with (left panels) and without (right panels) estuary discharge activated in the model. The simulated periods are 1.5–2.5 hours before (upper panels) and after (lower panels) a high spring tide and are forced with average wave conditions (H_s = 1 m, T_p = 12 s, D_p = 279°). Vectors represent virtual drifter tracks averaged over 1 hour onto 10 m spatial bins (every other bin shown for clarity). The 10 m spatial bin with the maximum seaward directed flow velocity defines U_{off} for the entire beach, while E is computed from the proportion of virtual drifters that exit the surfzone (Section 3.6). Contours indicate beach morphology (m ODN) while filled areas show submerged regions (blue) and breaker dissipation (white). Tidal stage is shown in the inset panels. Aerial imagery courtesy of National Network of Regional Coastal Monitoring Programmes of England, © 2024 NNRCMP.

4.6 Influence of beach morphology

Four different surveys of the sub- and inter-tidal bathymetry of the beach were conducted during May 2021, August 2021, May 2022, and July 2022 (Section 3.4). As Figure 12 shows, the morphology of the upper intertidal beach is dominated by the main river channel, which carves troughs >1 m deep in the beach face and evolves noticeably over the four surveys. In contrast, the lower beach contours remain relatively stable over this period, aside from slight variations in the ~1 m deep

headland boundary rip channels at either side of the beach, and the appearance and disappearance of smaller rip channels away from the headlands.

The main river channel enters the beach with a constant position along the northern headland before deflecting away from the headland towards the middle of the beach. Initially, this channel exits approximately through the middle of the beach
465 face (May 2021; Figure 12a), but in subsequent surveys the river channel is seen to shift periodically a few hundred meters southward (Aug 2021; Figure 12b) and northward (May 2022; Figure 12c). Less defined channels are also exhibited at various points in time, revealing relic positions of the main river channel.

XBeach simulations performed on the four different realisations of the morphology show that the variation in the spatial flow patterns over the four surveys is quite substantial (Figure 13, a-d), with the direction of the flows through the main river
470 channel varying by more than 45 degrees across the middle of the beach. Furthermore, the precise position of those strong channelised flows shifts over a distance of a few hundred meters. However, the hazard signature, here represented by U_{off} and E, is altered surprisingly little by the variations in the morphology (Figure 13, e-f). Over an average spring tide with average wave forcing ($H_s = 1$ m, $T_p = 12$ s, $D_p = 279°$), analysis of the virtual drifters suggests that the hazard signature is consistent across the four bathymetries, with seaward flows and surfzone exits maximised within 2 hours of high tide ($1 <$
475 $U_{off} < 1.4$ m/s; $30\% < E < 60\%$) and reduced seaward flows ($0.3 < U_{off} < 0.6$ m/s) predicted for the remainder of the tidal cycle, albeit with a second peak in exits occurring at low tide ($E \approx 20\%$). For a given tide level, the standard deviation in E and U_{off} across the four bathymetries is $\leq 8\%$ and ≤ 0.22 m/s, respectively, with maximum differences of up to 18% and 0.53 m/s, respectively. In comparison, the variation in E and U_{off} due to the tide moving over a single bathymetry is 60% and 1.2 m/s.

This suggests that temporal variation in the position and flow direction of the river channels due to the shifting morphology
480 does not significantly impact the overall hazard characteristics, and that for a given set of forcing conditions the variation in morphology plays a secondary role in the hazard level compared to the effect of varying the forcing conditions themselves. This relative insensitivity of the hazard level on beach morphology facilitates the development of a beach hazard prediction tool (Section 5), as frequent morphological updating is not required.
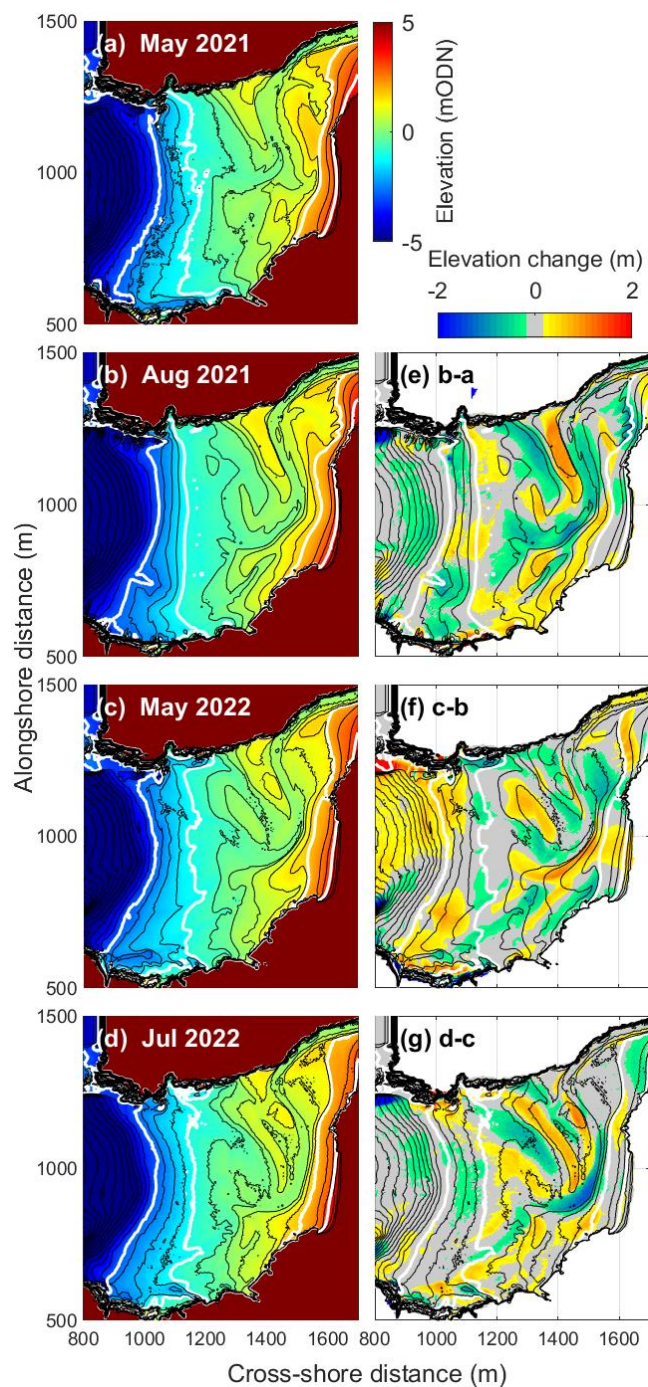
Figure 12: (a-d) Four different measured bathymetries at Crantock Beach (elevation mODN). (e-g) vertical elevation changes between surveys (m). The white lines in each panel show from l-r: Mean Low Water Spring, Mean Low Water Neap, Mean High Water Neap, and Mean High Water Spring contours.
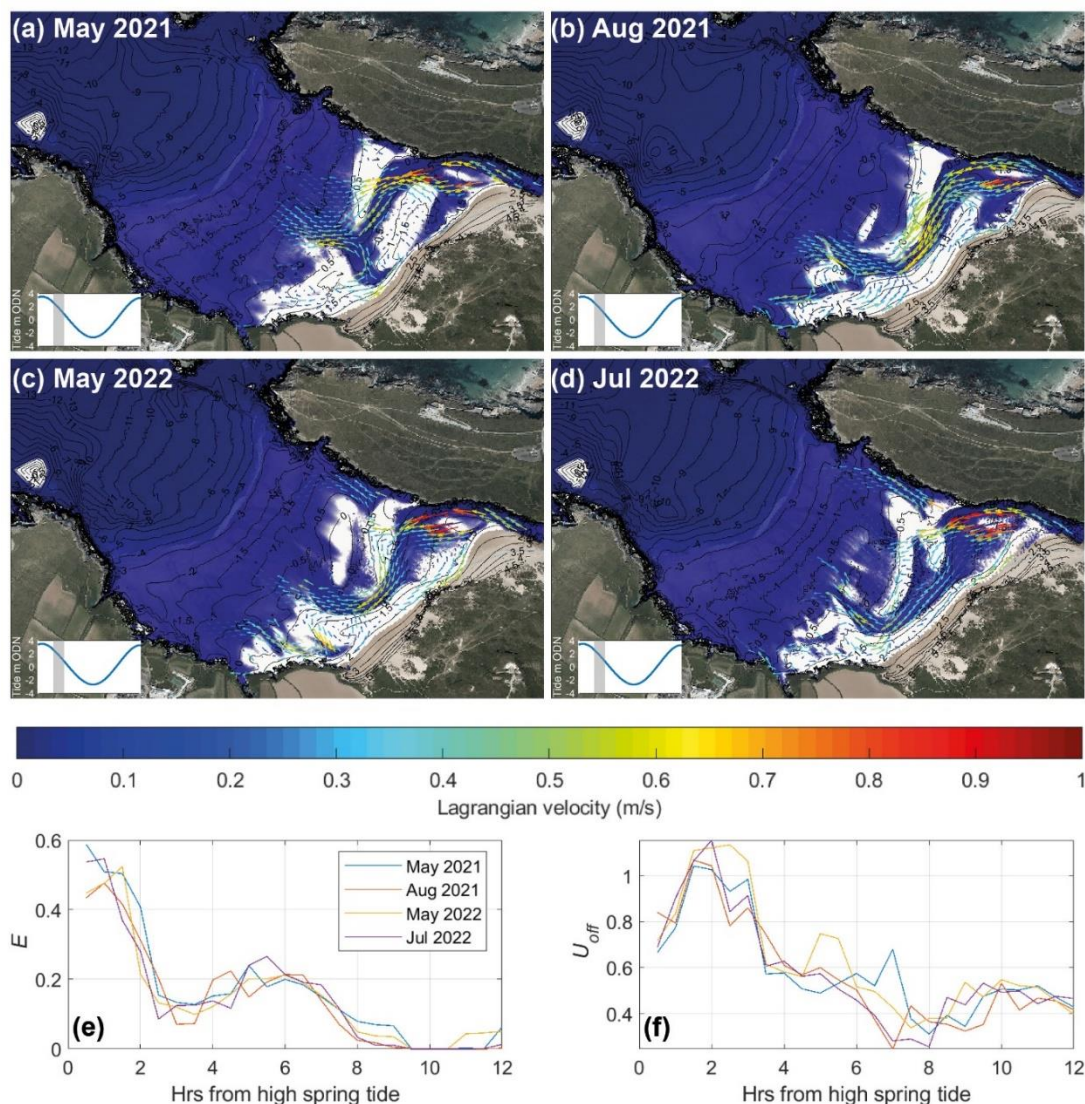
Figure 13: **(Panels a-d) Lagrangian surfzone circulation from XBeach run with four different measured bathymetries. The simulated periods are 1.5-2.5 hours after a high spring tide and are forced with average wave conditions (H_s = 1 m, T_p = 12 s, D_p = 279°). Vectors represent virtual drifter tracks averaged over 1 hour onto 10 m spatial bins (every other bin shown for clarity). Contours indicate beach morphology (m ODN) while filled areas show submerged regions (blue) and breaker dissipation (white). Tidal stage is shown in the inset panels. (Panel e) proportion of surfzone exits E and (Panel f) seaward flow velocity U_{off} predicted by XBeach over a spring tidal cycle forced with average wave conditions (H_s = 1 m, T_p = 12 s, D_p = 279°) over the four different bathymetries. Aerial imagery courtesy of National Network of Regional Coastal Monitoring Programmes of England, © 2024 NNRCMP.**

5 Forecasting bathing hazard

500   A site-specific bathing hazard forecast was developed for Crantock Beach in collaboration with the local landowners and the RNLI, with the intention of informing beach users of hazardous currents prior to accessing the beach. The calibrated XBeach model (Section 3.3) is used in the forecast system by initially running a suite of offline simulations and storing U_{off} and E from the model outputs in a look-up table to use as bathing hazard metrics. The simulations used to populate the database were carefully designed to cover the full range of summer wave and tide conditions, and optimise the computational effort

505   required to initially populate the hazard database (Section 3.5). Forecasted ocean wave and tide conditions at the boundary of the XBeach model are gathered each day from the open-source AMM15 models via the Copernicus Marine Environment Monitoring Service (CMEMS) API data server. These are compared using a nearest-neighbour search to the forcing in the look-up table, and a Hazard Score of 1–3 was applied to each timestep by comparing the predicted U_{off} and E values to simple thresholds (Table 1). The two scores from Table 1 were added together and rounded to achieve the final score,

510   following the approach of Austin et al. (2013).

To test the forecast system, Hazard Scores were assessed at times of flow-related bathing incidents (n = 648) recorded by the lifeguards at the beach over the years 2016–2021 (Figure 14). *Risk* is assessed using the total number of incidents over a given period. To estimate the probability of an individual water-user being involved in a flow-related incident (a proxy for the underlying level of *Hazard*), the data were discretised into 1-hour time bins and the number of incidents over each period

515   were divided by the instantaneous number of bathers (*Exposure*) counted by the lifeguards (Stokes et al., 2017; Scott et al., 2014; Wang and Sebastian, 2022). The highest hazard scores (HS2 and HS3) were forecasted most often (65% and 26% of the time, respectively) but also captured most of the observed *Risk* and *Hazard*. HS1 was forecasted least often (9%) but satisfactorily captured only 3% of the observed *Risk*, with a low average *Hazard* probability of 1-in-3,303 (Figure 14) and therefore represents a low *Risk*, low *Hazard* scenario. HS2 represents a high *Risk*, medium *Hazard* scenario capturing 57%

520   of past incidents with an average *Hazard* probability of 1-in-1,227. HS3 represents a high *Risk*, high *Hazard* scenario capturing 39% of past incidents with an average *Hazard* probability of 1-in-770. Hazard therefore increases by 2.7 times between HS1 and HS2, and increases by 1.6 times between HS2 and HS3.

Table 1. Hazard thresholds applied to seaward flow velocity U_{off} and proportion of exits E from each model simulation to calculate bathing hazard rating.

U_{off} (m/s)		$E(\%)$	
Threshold	Score	Threshold	Score
<0.2	0.5	<0.2	0.5
0.2-0.4	1	≥0.2	1.5
>0.4	1.5		
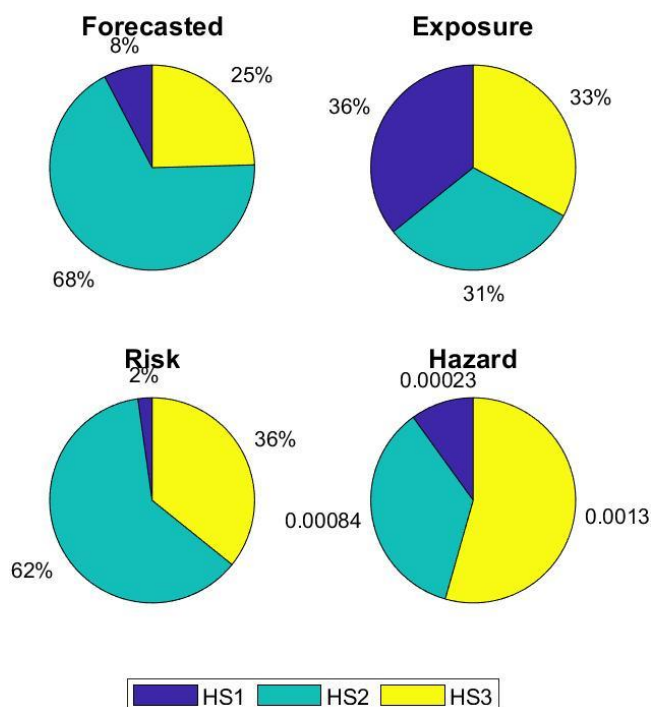
Figure 14: Performance summary of the developed bathing hazard forecast over the hindcast period (2016–2022). Proportion of forecasted Hazard Scores (HS1, HS2, HS3; upper left), relative average water-user exposure (upper right), proportion of total incidents (*Risk*, lower left), and probability of an individual water user being in a flow-related incident (*Hazard*, lower right).

6 Discussion

535 It is well known that strong flows can occur in estuaries, and they have previously been identified as hazardous locations for bathing, for example in Goa, India, by Chandramohan et al. (1997). In this study it has been shown that the presence of a large ebb delta on a macrotidal beach can lead to powerful and spatially complex surfzone flows. At Crantock the estuary is inactive below mid-tide, at which point surfzone currents consisted of onshore and alongshore wave driven flows and seaward flowing boundary rip currents (for example, Figure 8, upper panel), which exhibit velocities that are typical of rips

540 observed globally in other studies. For example, under a range of different wave conditions we predict wave-driven rip velocities of $U_{off} = 0.5$–1 m/s (Figure 10) during the lower half of the tide, which is in line with Lagrangian velocities of 0.4–1 m/s measured at microtidal, mesotidal, and macrotidal bar-rip beaches around the world (Scott et al., 2014; Austin et al., 2010; Macmahan et al., 2010; Mccarroll et al., 2017; Mccarroll et al., 2018). Similarly, the proportion of surfzone exits per hour that we predict when the estuary is inactive is on average $E = 15\%$ (range $E = 0$–42%), in line with global field and

545 modelling studies of morphologically-controlled rip currents that find average exits of $E = 14$–19% (range $E = 0$–34%) (Macmahan et al., 2010). Therefore, when the estuary is inactive, the bulk characteristics of the rip currents at this beach are no different from those observed at other beaches globally.

When the estuary is ebbing, however, the time-averaged surfzone velocities we measured and modelled reached $U_{off} = 1.5$ m/s, which is $\geq 50\%$ faster than typical velocities measured in channel rips (Austin et al., 2010; Scott et al., 2014; Macmahan

550 et al., 2010; Mccarroll et al., 2017; Mccarroll et al., 2018). Even boundary rip currents typically exhibit Lagrangian velocities below 1 m/s (Castelle and Coco, 2013; Mccarroll et al., 2014a), even under high-energy waves (Mouragues et al., 2020; Mouragues et al., 2021). The exit potential during the ebbing phase of the tide ($E \leq 62\%$) is also high, but is in line with observed and modelled wave-driven boundary rips from embayed beaches of a similar size (Mccarroll et al., 2014a; Castelle and Coco, 2013). The predominant oblique wave approach results in alongshore varying wave exposure, driving an

555 alongshore current towards the south headland where it deflects offshore. We find that considerably more surfzone exits occur either at the southern 'downstream' headland of Crantock (max $E = 90\%$) or at the northern 'upstream' headland (max $E = 72\%$) depending on the angle of wave approach, in line with previous findings (Castelle and Coco, 2013; Mccarroll et al., 2014a).

During the upper half of the tide, surfzone exits are maximised when wave power is below average, allowing the estuary to

560 ebb unhindered by waves, but exits decrease when wave conditions are more energetic than average ($W_f > 1$). When the estuary is flooding, surfzone exits cease completely, regardless of the level of wave energy. This suggests that surfzone exits at an estuary mouth beach are strongly controlled by both wave and estuary processes. While landward flows on the flood tide intuitively reduce the likelihood of material exiting the surfzone, waves breaking seaward of the ebb shoal delta under neap high tides and/or high wave energy ($W_f > 1$) can also reduce surfzone exits by increasing shoreward Stokes drift and

565 broken wave bores (Castelle et al., 2016) within the river channels. This is akin to breaker saturation on an outer sandbar reducing rip current exits through an inner bar at bar-rip beaches (Scott et al., 2014; Castelle et al., 2016). At Crantock, this

effect doesn't seem to occur during the lower tidal stages, however, with exits remaining at 15–20% for $1 < W_f < 4$, likely due to the well-defined boundary rip channels extending beyond the surfzone.

During both the ebbing and flooding high tide, the estuary dictates the flow velocity in the river channels (Figure 10).
570 Surprisingly, switching estuary discharge off in the model shows that wave-driven rip currents in the deep river channels could flow at a similar velocity to the strong currents that occur due to the estuary discharge itself (up to 1.5 m/s), even under average wave conditions (Section 4.5). This is significantly faster than would be expected from typical channel rips but fits with the concept posed by Mccarroll et al. (2018) that rip flow intensity is increased by shore-normal channels with high alongshore non-uniformity (i.e., deep and narrow), as is found in the river channel that cuts through the middle of Crantock
575 Beach. River channel morphology on a beach can therefore facilitate both strong estuary flows and strong rip current flows, regardless of estuarine discharge. Furthermore, the channels efficiently convey water towards wave-driven rip currents further down the beach, linking flows across the surfzone and providing a conveyor belt to transport bathers from the shore to deeper water offshore.

Channel rips have been observed globally to increase in intensity at low tide as a result of flow constriction through low-tide
580 bar-rip channels and/or increased intensity of wave breaking over sandbars (Castelle et al., 2016; Aagaard et al., 1997; Brander and Short, 2001; Macmahan et al., 2006; Macmahan et al., 2005). As a result, low tide levels have been linked with higher occurrence of bathing incidents (Koon et al., 2023; Scott et al., 2014; Castelle et al., 2019) and drowning risk (Koon et al., 2023). In contrast, here we find a mechanism for dangerous seaward flows to occur during the high tide phase, either from estuary discharge or high tide 'river channel rips'. While the efficacy of these high-tide rips was sensitive to the estuary
585 discharge, they were present whether the estuary was ebbing or flooding (for example, Figure 9). Koon et al. (2023) found that on Australian beaches, there was no link between tidal phase or tide range, and coastal drownings. However, here we demonstrate a clear difference in bathing hazard during rising and falling stages of the tide when an estuary mouth is involved, albeit in a location with a much larger tidal excursion. During the upper half of the tidal cycle, hazard is strongly controlled by tidal phase, range, water level, and wave conditions, while during the lower half of the tidal cycle only water
590 level and wave conditions appear to be important.

Rip current forecasts have been developed in several previous studies. Some of these systems operate at a regional/national scale using data-driven empirical relationships that link forecasted wave, tide, and weather conditions to lifeguard rescue statistics (Scott et al., 2022; Lushine, 1991; Lascody, 1998; Engle et al., 2002; Dusek and Seim, 2013; Gibbs et al., 2015). Other studies have developed site-specific calibrated process-based models to predict where and when rip current activity
595 will occur on a beach (Austin et al., 2013; Kim et al., 2013; Mccarroll et al., 2018; Mccarroll et al., 2015), but these have rarely been applied operationally and none have yet included dynamics from channel rips, boundary rips, and estuary flow. The forecast system developed for Crantock has been implemented operationally at the beach since 2022 (Figure 15) and provides real-time warnings about where and when peak bathing hazards will occur via novel digital display screens located at the two main beach access points. To the best of our knowledge, this represents the first detailed hydrodynamic
600 forecasting system used to provide warnings directly to the public. Work is now underway to better understand whether such

warning systems are effective at influencing and informing beach user decision-making, and therefore contribute to a reduction in life risk.
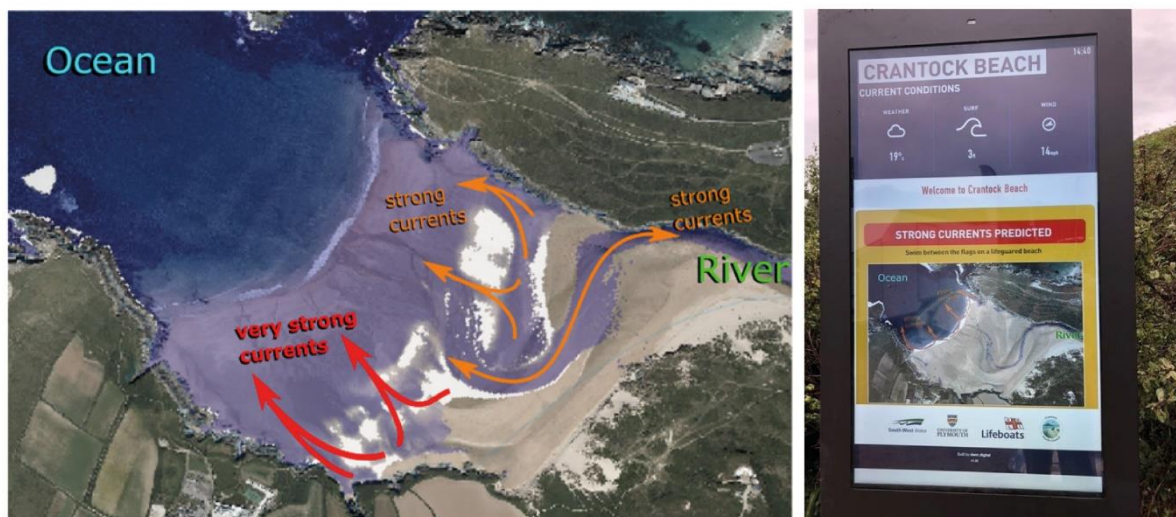
605 **Figure 15: (Left panel) example of simplified beach hazards information derived from simulated drifter patterns. (Right panel) operational digital bathing hazards sign at Crantock Beach next to a key beach access point showing dynamic hazard predictions for the next hour. Aerial imagery courtesy of National Network of Regional Coastal Monitoring Programmes of England, © 2024 NNRCMP.**

610

7 Conclusions

Surfzone currents at an embayed estuary mouth beach were both measured and modelled, revealing complex surfzone circulation patterns, including circulating, alongshore, and exiting flow regimes. The river channel morphology is a key

615 driver of the circulation above mid-tide. The river channels act to constrain both estuarine and wave-driven currents, directing the flows alongshore and offshore, often connecting with boundary and channel rip currents lower on the beach face. Flow velocities through the river channels were enhanced by increasing estuary discharge, increasing wave power, and decreasing water depth.

The most hazardous flows are predicted to occur during ebbing high spring tides with wave power at or below average, when

620 estuary discharge and wave driven return flows can flow seaward through the river channels unhindered by the surfzone. Under such conditions, the highest seaward velocities (up to 1.5 m/s) and maximum potential for surfzone exits (> 60%) occurred. While wave-driven channel rips have been widely observed to occur preferentially over low tide bar-rip morphology, we present a novel mechanism for 'river channel rips' to occur near high tide due to wave breaking over an ebb-shoal delta, which can drive seaward return flows in the adjacent river channels, even in the absence of estuary discharge.

625 The combined action of estuary and wave-driven flows on this beach generates seaward currents that are up to 50% faster than peak rip current velocities observed in the literature and are combined with very high surfzone exit rates. This indicates that the presence of an estuary mouth within an energetic surfzone poses a highly hazardous situation for bathers which was previously unstudied in the literature, despite potentially exceeding the hazard that would be expected from rip currents alone. Surprisingly, despite significant spatio-temporal variability in the position of the river channels on the beach face, it

630 was found to be possible to predict the timing and severity of past bathing incidents from model simulations, providing a means to simulate and forecast bathing hazards to forewarn bathers about times of peak bathing hazard.

Competing interests

The contact author has declared that none of the authors has any competing interests.

References

635 Aagaard, T., Greenwood, B., and Nielsen, J.: Mean currents and sediment transport in a rip channel, Mar. Geol., 140, 25-45, https://doi.org/10.1016/s0025-3227(97)00025-x, 1997.
Allen, G. P.: Relationship between grain size parameter distribution and current patterns in the Gironde estuary (France), J. Res., 41, 74-88, https://doi.org/10.1306/74d721ee-2b21-11d7-8648000102c1865d, 1971.
Austin, M., Scott, T., Brown, J., MacMahan, J., Masselink, G., and Russell, P.: Temporal observations of rip current

640 circulation on a macrotidal beach, Cont. Res., 30, 1149-1165, https://doi.org/10.1016/j.csr.2010.03.005, 2010.
Austin, M. J., Scott, T. M., Russell, P. E., and Masselink, G.: Rip current prediction: Development, validation, and evaluation of an operational tool, J. Res., 29, 283-300, https://doi.org/10.2112/jcoastres-d-12-00093.1, 2013.
Barnard, P. L. and Warrick, J. A.: Dramatic beach and nearshore morphological changes due to extreme flooding at a wave-dominated river mouth, Mar. Geol., 271, 131-148, https://doi.org/10.1016/j.margeo.2010.01.018, 2010.

645   Brander, R. W.: Field observations on the morphodynamic evolution of a low-energy rip current system, Mar. Geol., 157, 199-217, https://doi.org/10.1016/s0025-3227(98)00152-2, 1999.

Brander, R. W. and Short, A. D.: Flow kinematics of low-energy rip current systems, J. Res., 468-481, 2001.

Brighton, B., Sherker, S., Brander, R., Thompson, M., and Bradstreet, A.: Rip current related drowning deaths and rescues in Australia 2004–2011, Natural Hazards and Earth System Science, 13, 1069-1075, https://doi.org/10.1136/injuryprev-2012-
650   040580g.17, 2013.

Castelle, B. and Coco, G.: The morphodynamics of rip channels on embayed beaches, Cont. Res., 43, 10-23, https://doi.org/10.1016/j.csr.2012.04.010, 2012.

Castelle, B. and Coco, G.: Surf zone flushing on embayed beaches, Geophys. Lett., 40, 2206-2210, https://doi.org/10.1002/grl.50485, 2013.

655   Castelle, B., Scott, T., Brander, R. W., and McCarroll, R. J.: Rip current types, circulation and hazard, Earth. Rev., 163, 1-21, https://doi.org/10.1016/j.earscirev.2016.09.008, 2016.

Castelle, B., Scott, T., Brander, R., McCarroll, J., Robinet, A., Tellier, E., Korte, E. d., Simonnet, B., and Salmi, L.-R.: Environmental controls on surf zone injuries on high-energy beaches, Nat. Sys., 19, 2183-2205, https://doi.org/10.5194/nhess-19-2183-2019, 2019.

660   Castelle, B., Michallet, H., Marieu, V., Leckler, F., Dubardier, B., Lambert, A., Berni, C., Bonneton, P., Barthélemy, E., and Bouchette, F.: Laboratory experiment on rip current circulations over a moveable bed: Drifter measurements, Journal of Geophysical Research: Oceans, 115, https://doi.org/10.1029/2010jc006343, 2010.

Chandramohan, P., Kumar, V. S., and Jena, B.: Rip current zones along beaches in Goa, west coast of India, Journal of waterway, port, coastal, and ocean engineering, 123, 322-328, https://doi.org/10.1061/(asce)0733-950x(1997)123:6(322),
665   1997.

Cooper, J. A. G.: Geomorphological variability among microtidal estuaries from the wave-dominated South African coast, Geomorphology. Geomorphology., 40, 99-122, https://doi.org/10.1016/S0169-555X(01)00039-3, 2001.

Daly, C., Roelvink, D., van Dongeren, A., de Vries, J. v. T., and McCall, R.: Validation of an advective-deterministic approach to short wave breaking in a surf-beat model, Coast. Eng., 60, 69-83,
670   https://doi.org/10.1016/j.coastaleng.2011.08.001, 2012.

Dudkowska, A., Boruń, A., Malicki, J., Schönhofer, J., and Gic-Grusza, G.: Rip currents in the non-tidal surf zone with sandbars: numerical analysis versus field measurements, Oceanologia. Oceanologia., 62, 291-308, https://doi.org/10.1016/j.oceano.2020.02.001, 2020.

Dusek, G. and Seim, H.: A probabilistic rip current forecast model, J. Res., 29, 909-925, https://doi.org/10.2112/jcoastres-d-
675   12-00118.1, 2013.

Engle, J., MacMahan, J., Thieke, R. J., Hanes, D. M., and Dean, R. G.: Formulation of a Rip Current Predictive Index Using Rescue Data, 2002 national conference on beach preservation technology,

Gibbs, A., Dusek, G., Van der Westhuysen, A., Santos, P., Huddleston, S., Estupiñan, J., Rivera, E., Stripling, S., and Padilla, R.: P 3.5 Numerical Validation of a Coupled Probabilistic Rip Current Model and Nearshore Wave Prediction
680   System For South Florida, 2015.

Groeneweg, J. and Klopman, G.: Changes of the mean velocity profiles in the combined wave–current motion described in a GLM formulation, J. Mech., 370, 271-296, https://doi.org/10.1017/s0022112098002018, 1998.

Hartanto, I. M., Beevers, L., Popescu, I., and Wright, N. G.: Application of a coastal modelling code in fluvial environments, Environ. Softw., 26, 1685-1695, https://doi.org/10.1016/j.envsoft.2011.05.014, 2011.

685   Hird, S., Stokes, C., and Masselink, G.: Emergent coastal behaviour results in extreme dune erosion decoupled from hydrodynamic forcing, Mar. Geol., 442, 106667, https://doi.org/10.1016/j.margeo.2021.106667, 2021.

Hume, T. M. and Herdendorf, C. E.: A geomorphic classification of estuaries and its application to coastal resource management—a New Zealand example, Ocean and Shoreline Management, 11, 249-274, https://doi.org/10.1016/0951-8312(88)90022-7, 1988.

690   Hume, T. M., Snelder, T., Weatherhead, M., and Liefting, R.: A controlling factor approach to estuary classification, Ocean. Manage., 50, 905-929, https://doi.org/10.1016/j.ocecoaman.2007.05.009, 2007.

Jiang, A. W., Ranasinghe, R., and Cowell, P.: Contemporary hydrodynamics and morphological change of a microtidal estuary: a numerical modelling study, Ocean. Dynam., 63, 21-41, https://doi.org/10.1007/s10236-012-0583-z, 2013.

Kench, P. S.: Geomorphology of Australian estuaries: review and prospect, Aust. Ecol., 24, 367-380,
695   https://doi.org/10.1046/j.1442-9993.1999.00985.x, 1999.

Kim, I., Lee, J., and Lee, J.: Verification of rip current simulation using a two-dimensional predictive model, HAECUM, J. Res., 726-730, https://doi.org/10.2112/si65-123.1, 2013.

Koon, W., Brander, R. W., Dusek, G., Castelle, B., and Lawes, J. C.: Relationships between the tide and fatal drowning at surf beaches in New South Wales, Australia: Implications for coastal safety management and practice, Ocean. Manage., 238,
700   106584, https://doi.org/10.1016/j.ocecoaman.2023.106584, 2023.

Lascody, R. L.: East central Florida rip current program, National Weather Digest, 22, 25-30, 1998.

Lessa, G. and Masselink, G.: Morphodynamic evolution of a macrotidal barrier estuary, Mar. Geol., 129, 25-46, https://doi.org/10.1016/0025-3227(95)00103-4, 1995.

Lippmann, T. C. and Holman, R. A.: The spatial and temporal variability of sand bar morphology, J. Res., 95, 11575-11590,
705   https://doi.org/10.1029/jc095ic07p11575, 1990.

Longuet-Higgins, M. S. and Stewart, R. W.: Radiation stress and mass transport in gravity waves, with application to 'surf beats', J. Mech., 13, 481-504, https://doi.org/10.1017/s0022112062000877, 1962.

Longuet-Higgins, M. S. and Stewart, R. W.: Radiation stresses in water waves; a physical discussion, with applications, Deep Sea Research and Oceanographic Abstracts, 11, 529-562, https://doi.org/10.1016/0011-7471(65)90982-4, 1964.

710   Lushine, J. B.: A study of rip current drownings and related weather factors, National weather digest, 16, 13-19, 1991.

MacMahan, J., Reniers, A., Brown, J., Brander, R., Thornton, E., Stanton, T., Brown, J., and Carey, W.: An introduction to rip currents based on field observations, J. Res., 27, 3-6, https://doi.org/10.2112/jcoastres-d-11-00024.1, 2011.

MacMahan, J., Brown, J., Brown, J., Thornton, E., Reniers, A., Stanton, T., Henriquez, M., Gallagher, E., Morrison, J., and Austin, M. J.: Mean Lagrangian flow behavior on an open coast rip-channeled beach: A new perspective, Mar. Geol., 268, 1-
715   15, https://doi.org/10.1016/j.margeo.2009.09.011, 2010.

MacMahan, J. H., Thornton, E. B., and Reniers, A. J. H. M.: Rip current review, Coast. Eng., 53, 191-208, https://doi.org/10.1016/j.coastaleng.2005.10.009, 2006.

MacMahan, J. H., Thornton, E. B., Stanton, T. P., and Reniers, A. J.: RIPEX: Observations of a rip current system, Mar. Geol., 218, 113-134, https://doi.org/10.1016/j.margeo.2005.03.019, 2005.

720   Masselink, G. and Short, A. D.: The effect of tide range on beach morphodynamics and morphology: a conceptual beach model, J. Res., 9, 785-800, 1993.

Masselink, G., Brooks, S., Poate, T., Stokes, C., and Scott, T.: Coastal dune dynamics in embayed settings with sea-level rise–Examples from the exposed and macrotidal north coast of SW England, Mar. Geol., 450, 106853, https://doi.org/10.1016/j.margeo.2022.106853, 2022.

725   Masselink, G., Scott, T., Poate, T., Russell, P., Davidson, M., and Conley, D.: The extreme 2013/2014 winter storms: hydrodynamic forcing and coastal response along the southwest coast of England, Earth Surface Processes and Landforms, 41, 378-391, https://doi.org/10.1002/esp.3836, 2016.

McCarroll, R. J., Brander, R., and Scott, T.: Wave height and bathymetric controls on surfzone current velocity and dispersion across an embayed beach, Coastal Dynamics, 431-442,
730   McCarroll, R. J., Brander, R. W., Scott, T., and Castelle, B.: Bathymetric controls on rotational surfzone currents, Journal of Geophysical Research: Earth Surface, 123, 1295-1316, https://doi.org/10.1029/2017jf004491, 2018.

McCarroll, R. J., Castelle, B., Brander, R. W., and Scott, T.: Modelling rip current flow and bather escape strategies across a transverse bar and rip channel morphology, Geomorphology. Geomorphology., 246, 502-518, https://doi.org/10.1016/j.geomorph.2015.06.041, 2015.

735   McCarroll, R. J., Brander, R. W., Turner, I. L., Power, H. E., and Mortlock, T. R.: Lagrangian observations of circulation on an embayed beach with headland rip currents, Mar. Geol., 355, 173-188, https://doi.org/10.1016/j.margeo.2014.05.020, 2014a.

McCarroll, R. J., Brander, R. W., MacMahan, J. H., Turner, I. L., Reniers, A. J. H. M., Brown, J. A., Bradstreet, A., and Sherker, S.: Evaluation of swimmer-based rip current escape strategies, Nat. Hazards., 71, 1821-1846,
740   http://dx.doi.org/10.1016/j.geomorph.2015.06.041, 2014b.

Mouragues, A., Bonneton, P., Castelle, B., and Martins, K.: Headland Rip Modelling at a Natural Beach under High-Energy Wave Conditions, Journal of Marine Science and Engineering, 9, 1161, https://doi.org/10.3390/jmse9111161, 2021.

Mouragues, A., Bonneton, P., Castelle, B., Marieu, V., Jak McCarroll, R., Rodriguez-Padilla, I., Scott, T., and Sous, D.: High-energy surf zone currents and headland rips at a geologically constrained mesotidal beach, Journal of Geophysical Research: Oceans, 125, e2020JC016259, https://doi.org/10.1029/2020jc016259, 2020.

745 Nairn, R. B., Roelvink, J. A., and Southgate, H. N.: Transition zone width and implications for modelling surfzone hydrodynamics, Coast. Eng., 68-81, https://doi.org/10.1061/9780872627765.007, 1991.

Nordstrom, K. F.: Estuarine beaches: an introduction to the physical and human factors affecting use and management of beaches in estuaries, lagoons, bays and fjords, Springer Science & Business Media1992.

750 Phillips, O. M.: The dynamics of the upper ocean, 2nd, Cambridge University Press, New York1977.

Pye, K. and Blott, S. J.: The geomorphology of UK estuaries: The role of geological controls, antecedent conditions and human activities, Estuarine, Coastal and Shelf Science, 150, 196-214, https://doi.org/10.1016/j.ecss.2014.05.014, 2014.

Reniers, A. J., MacMahan, J., Thornton, E., Stanton, T. P., Henriquez, M., Brown, J., Brown, J., and Gallagher, E.: Surf zone surface retention on a rip-channeled beach, Journal of Geophysical Research: Oceans, 114, https://doi.org/10.1029/2008jc005153, 2009.

755 Roelvink, D. and Reniers, A.: A guide to modeling coastal morphology, in: Advances in Coastal Engineering, world scientific, Singapore, 2011.

Roelvink, D., McCall, R., Mehvar, S., Nederhoff, K., and Dastgheib, A.: Improving predictions of swash dynamics in XBeach: The role of groupiness and incident-band runup, Coast. Eng., 134, 103-123, https://doi.org/10.1016/j.coastaleng.2017.07.004, 2018.

760 Roelvink, D., Reniers, A., Van Dongeren, A., Van Thiel de Vries, J., Lescinski, J., and McCall, R.: XBeach model description and manual, Delft University of Technology, User Manual, Delft, The Netherlands, 2010.

Roelvink, D. R., A.: Dissipation in random wave groups incident on a beach, Advances in Coastal Engineering, 19, 127-150, https://doi.org/10.1016/0378-3839(93)90021-y, 1993.

765 Roy, P.: New South Wales estuaries: their origin and evolution, Coastal geomorphology in Australia, 1984.

Scott, T., Masselink, G., and Russell, P.: Morphodynamic characteristics and classification of beaches in England and Wales, Mar. Geol., 286, 1-20, https://doi.org/10.1016/j.margeo.2011.04.004, 2011.

Scott, T., Austin, M., Masselink, G., and Russell, P.: Dynamics of rip currents associated with groynes—field measurements, modelling and implications for beach safety, Coast. Eng., 107, 53-69, https://doi.org/10.1016/j.coastaleng.2015.09.013,

770 2016.

Scott, T., Masselink, G., Austin, M. J., and Russell, P.: Controls on macrotidal rip current circulation and hazard, Geomorphology. Geomorphology., 214, 198-215, https://doi.org/10.1016/j.geomorph.2014.02.005, 2014.

Scott, T., Masselink, G., Stokes, C., Poate, T., Wooler, A., and Instance, S.: A 15-year partnership between UK coastal scientists and the international beach lifeguard community, Cont. Res., 241, 104732,

775 https://doi.org/10.1016/j.csr.2022.104732, 2022.

Scott, T. M., Russell, P. E., Masselink, G., Wooler, A., and Short, A.: High volume sediment transport and its implications for recreational beach risk, Proceedings 31st International Conference on Coastal Engineering, ASCE, Hamburg, Germany, 4250-4262, https://doi.org/10.1142/9789814277426_0353,

Stokes, C., Masselink, G., Revie, M., Scott, T., Purves, D., and Walters, T.: Application of multiple linear regression and

780 Bayesian belief network approaches to model life risk to beach users in the UK, Ocean and Coastal Management, 139, 12-23, https://doi.org/10.1016/j.ocecoaman.2017.01.025, 2017.

Svendsen, I. A.: Wave heights and set-up in a surf zone, Coast. Eng., 8, 303-329, https://doi.org/10.1016/0378-3839(84)90028-0, 1984.

Wang, Y. V. and Sebastian, A.: Equivalent hazard magnitude scale, Nat. Sys., 22, 4103-4118,

785 https://doi.org/10.21203/rs.3.rs-117402/v1, 2022.

Wright, L. D. and Short, A. D.: Morphodynamic variability of surf zones and beaches: A synthesis, Mar. Geol., 56, 93-118, https://doi.org/10.1016/0025-3227(84)90008-2, 1984.